CHARACTERIZATION OF NON-VOLATILE PARTICULATE MATTER IN PRESSURIZED PREMIXED LAMINAR JET-A FLAMES VIA THERMOPHORETIC SAMPLING

A Dissertation
Presented to
The Academic Faculty

By

Sundar Ram Manikandan

In Partial Fulfillment
of the Requirements for the Degree of
Master of Science in
Aerospace Engineering
Daniel Guggenheim School of Aerospace Engineering

Georgia Institute of Technology

August 2022

CHARACTERIZATION OF NON-VOLATILE PARTICULATE MATTER IN PRESSURIZED PREMIXED LAMINAR JET-A FLAMES VIA THERMOPHORETIC SAMPLING

Thesis committee:

Dr. Adam Michael Steinberg, Advisor
School of Aerospace Engineering
Georgia Institute of Technology

Dr. Ellen Yi Chen Mazumdar
School of Mechanical Engineering
Georgia Institute of Technology

Dr. Wenting Sun
School of Aerospace Engineering
Georgia Institute of Technology

Date approved: August 9, 2022

ACKNOWLEDGMENTS

Dr. Adam Steinberg, I cannot begin to express my sincere gratitude and appreciation for you. Thank you for providing me with the guidance and counsel that I needed to complete this thesis. Your inputs and critiques helped me understand, and write better. I am extremely grateful to you for giving me the opportunity to work on several projects.

Speaking of constructive criticism, I'd like to extend my gratitude to the thesis review committee: Dr. Ellen Mazumdar and Dr. Wenting Sun, whose inputs from the proposal helped me get a comprehensive, yet cogent study. I appreciate you taking your time to give me valuable feedback. Special thanks to Dr. Ding Yong, who helped me with operating the TEM. Finally, I cannot leave Georgia Tech without thanking Dr. Jerry Seitzman. Your inputs during setting grad lab up, and grading the reports are highly valued.

And now to the people that I spent most of my grad school with (1) Sam & Andy- the colleagues who became friends; bonding over our unified desperation (& efforts) to get the burner up and running, spontaneously deciding to have food outside, hiking, etc., we managed to find a balanced approach the test-rig operational; and obtained a fascinating flame, congratulations to us! We never really took a moment to thank all the shattered windows to realize that simple hand-tightening was just enough to hold pressure. Their coerced sacrifice shall not be forgotten!; (2) Akshith, Tarun, Vedant, Keshav, Anirudh, Nikhil, Krithika & Swetha- Thank you all for the time spent playing games, movies, trips (planned around food) and random drives; and lastly, to the friends that helped me adapt to the new country in a flash (3) Manya, Julia, Akshay, and (especially) Nikhit- I understand that signing up for the first sub-lease was on both of us; but from the second one onward, you bought that on yourself!

Finally, the family- you got pushed to the last, yet again! As much as I don't say this out a lot, I am extremely grateful for you and your unconditional love and support.

TABLE OF CONTENTS

LIST OF FIGURES

LIST OF ACRONYMS

CST Civil Supersonic Transportation

HAB Height Above the Burner

HRTEM High-Resolution Transmission Electron Microscopy

LFB Laminar Flame Burner

LII Laser Induced Incandescence

LPP Lean Prevaporized Premixed

LRTEM Low-Resolution Transmission Electron Microscopy

PAH Poly Aromatic Hydrocarbon

PDF Probability Density Function

SA Sampler Assembly

TEM Transmission Electron Microscope

TiRe Time-Resolved

TSS Thermophoretic Soot Sampling

SUMMARY

Production and subsequent emissions of non-volatile particulate matter (nvPM) pose a challenge for both optical diagnostics and physical probing, especially at conditions relevant to practical combustors. Key to enabling nvPM mitigation is *in-situ* optical measurements, particularly laser induced incandescence (LII). However, interpreting the LII signals is challenging. To quantitatively use LII in gas turbines, their measurements must be calibrated and validated against physical nvPM samples. The preferred approach for extracting these physical samples is *in-situ* thermophoretic soot sampling followed by transmission electron microscope (TEM) imaging.

This thesis work deals with the design of a multi-probe thermophoretic soot sampling system capable of extracting nvPM samples in laminar, rich flames of prevaporized jet-A/air premixtures at elevated pressures. The flames under investigation were observed to exhibit thermal-diffusive instabilities, that are responsible for the flame to form corrugated structures. Moreover, these instabilities cause the corrugated flame to exhibit spatio-temporal variations, which exacerbate the challenges in implementing diagnostics. For the soot sampler, a significantly larger sampling time of 125 ms was required to obtain sufficient soot deposition on the TEM grids, which can enhance the extent of restructuring in the deposited soot particles.

Visualization of the data through the TEM revealed (i) a wide range of soot particle size varying between 10 – 250 nm; (ii) presence of non-soot organic matters that include (1) fibers, (2) sharp contrasted mineral-like structures, and (3) uniform and porous spherical structures with varying contrast; and (iii) the dominant morphological characteristics of the flame generated soot particles that are indicative of its chemically reactive nature and restructuring. Furthermore, the quantitative results show (i) increasing soot particle size with pressure, and (ii) an increasing-decreasing trend for the mean soot particle size with height above the burner. While the effect of pressure is explained by the enhanced extent

of graphitization and maturity in the nanostructures of soot particles at elevated pressures; the dependence on height can be explained through particle agglomeration for the initial increase in size with height, followed by oxidation of the particles respectively. However, considering the range of tested HAB when compared to the flame length, the possibility for inconclusive variation stems from preheat temperature variations and restructuring effects.

CHAPTER 1

INTRODUCTION

1.1 Motivation

Non-volatile particulate matter (nvPM)/carbon black/soot production is a commonly observed phenomenon in gas turbine combustors. Soot particles are formed when long chains of Poly Aromatic Hydrocarbon (PAH) nucleate, conglomerate and roll over to form spherical structures. These particles luminesce at high temperatures (1500 K), which is observed as an orange/yellow shade in the flame (Figure 1.1). Heavy fuels like gasoline, diesel, and aviation kerosene contain aromatic species and, therefore, readily produce PAH and soot particles. These emissions play a detrimental role in the combustion efficiency of gas turbines, as they increase the radiative heat losses. This heat loss not only reduces the combustion gas temperatures, but also damages the combustor liner, thereby reducing its durability. Moreover, the presence of carbonaceous soot is indicative of incomplete combustion.

Figure 1.1: Soot formation in a laminar jet-A air flame

Beyond its detrimental effects on the engine, the emission of soot is also a significant contributor to climate change [1, 2]. The Inter-Governmental Panel on Climate Change (IPCC) estimates the direct effect of carbon soot by global climate forcing due to fossil fuel black carbon aerosols as 0.2 W/m^2. Optical and electron microscopes show the presence of soot and aerosols in snow, a dominant effect on snow/ice albedo [3] is estimated to be around 0.8 W/m^2. Moreover, soot has other detrimental environmental effects beyond climate change, for example contamination of fresh water [3].

Several studies from the World Health Organization (WHO) demonstrate the effect of exhaust emissions public health. Stettler et al. [1] produced an inventory of emissions from airports in the United Kingdom that include emissions due to aircrafts takeoff and landings. The most recent review on gas turbine emission exposure has been performed by Bendsten et. al [4]. This study focuses on the correlation between non-volatile exhaust emissions to diagnoses of respiratory symptoms, ischemic heart disease, and cerebrovascular disease. It was concluded that the jet engine particulate emissions have physiochemical properties similar to diesel exhaust particles and share similar adverse health effects. The severity of the impact of soot on climate change and public health [2–5] necessitates the creation and enforcement of strict emissions regulations, which presents an additional challenge in combustor design. In order to mitigate soot emissions and its detrimental impacts, it is necessary to understand the processes by which it is formed in gas turbine combustion. Furthermore, interest in the formation, and partial or complete oxidation of soot in flames stems from the need for greater efficiency in conversion of chemical energy and for improved control for air pollution [6].

There is increasing interest in Lean Prevaporized Premixed (LPP) combustors burning Jet A fuel for Civil Supersonic Transportation (CST). Soot formation in these systems, particularly at cruise, is of interest due both to the high altitudes at which such airplanes would fly and the rather unusual conditions at which the combustors operate. Design and deployment of physical probes in a typical gas turbine combustor environment is challenging, and

most importantly intrusive in nature. Thus, the ideal techniques to study soot formation in a gas turbine combustor are in-situ laser diagnostics, particularly Laser Induced Incandescence (LII). However, the complexities associated with the interpretation of the LII signal mandate the need for pre-calibration and validation.

In the past, sooting flames have predominantly been studied in rich diffusion flames at atmospheric conditions [7–11] though several studies have been performed on diffusion flames at elevated pressures as well [12–15]. Relatively few studies have characterized soot formation in premixed flames. The effect of pressure on soot production and its diagnostics is of interest in premixed flames, because of its relevance in LPP combustors. Therefore, the main objective of this investigation is to simultaneously collect physical soot samples and Time-Resolved (TiRe) LII data; and analyze particle size distribution in rich, pre-vaporized, premixed, laminar jet-A flames at elevated pressures. Moreover, the size distribution data also can be used as: (i) prior for bayesian analysis based LII signal post-processing, (ii) validation of numerical simulations, etc. In order to achieve this objective and understand the morphological characteristics of nvPM, a soot sampling system is designed and deployed to sample the soot particles at various locations in the flame.

1.2 Literature Review

Soot is produced by incomplete combustion of carbaneceous materials, therefore it typically occurs in a fuel rich zone. In a premixed combustor, a homogenous mixture of fuel and oxidizer is obtained in the upstream of the reaction zone. So for a premixed flame, a rich unburnt gas mixture is required to produce soot. The premixed flames of heavy fuel, under these conditions, have intrinsic instabilities that are responsible for the flames forming unusual structures on the combustion surface [16]. These inherent instabilities associated with the flame complicate the implementation of combustion diagnostics.

1.2.1 Structure of Premixed Flames

It is known that formation of cellular features are an inseparable feature of premixed flame containing thermal diffusive instabilities. For a flat flame, the bulk consists of individual cellular flames that bulge towards the unburnt mixture. The intercellular space is dark, which indicates lack of chemical reactions. The manifestation of these cellular instabilities is dependent on differential diffusion, flame stretch and the downstream heat loss. For Bunsen flames, these instabilities cause the flame to split into triangular flamelets. The number of such flamelets depend on the circumference of burner nozzle and these structures exhibit spatio-temporal variations. Typically, they form polyhedral pyramids (see Figure 1.2a) that remain stationary for some conditions, and rotate about the vertical axis for slight changes in gas compositions and velocity [16, 17]. The formation of these structures is affected by the aerodynamics in the vicinity of the nozzle tip, i.e. (i) burner entraining air are unable to produce polyhedral flamelets; and (ii) increasing nitrogen co-flow increases the propensity to form such structures [17].

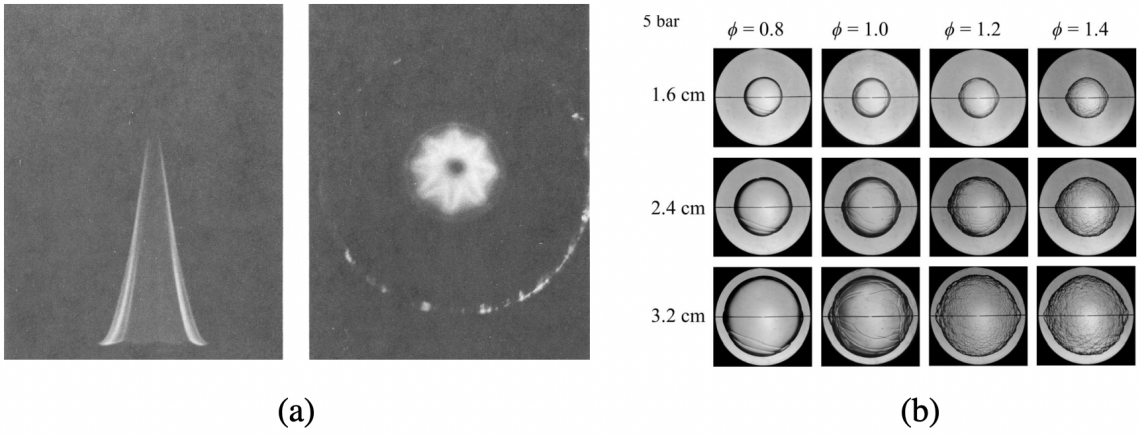

Figure 1.2: Thermal diffusive instabilities in rich-premixed flames of heavy fuel: (a) Butane bunsen flame [17]; (b) Butanone spherical [18].

Formation of these cellular structures, as shown in Figure 1.2, is the direct effect of preferential (differential) diffusion, which also can have stabilizing effects depending on the mobility of limiting species. These instabilities manifest in fuel-oxidizer mixtures that are

deficient in the light reactants (for example, rich mixtures of heavy fuels or lean mixtures of light fuels), i.e. when the Lewis number of the deficient reactant is smaller than some critical value [19].

Law [20] observed the presence of different types of flame front instabilities for premixed hydrocarbon fuel-based flames as (i) cellular flame, (ii) star-shaped flame, (iii) groove-shaped, and (iv) vibrating flame. It was noted that the cellular and star shaped flames are caused by preferential diffusion. While the cellular instabilities are dominant in flat flames, increasing stretch dampens the instabilities in the direction of stretch. This suppresses the radial instabilities in a negatively stretched (Bunsen) flame, thus forming a star-shaped pattern. Additional stretch is expected to further suppresses these star-shaped instabilities, which causes the flamelets to amalgamate into a cohesive flame structure. While the groove shaped instabilities are a coupled effect of differential diffusion and flame aerodynamics, the vibrational mode of instabilities result from unsteady downstream heat loss [20–22].

1.2.2 Soot Formation Process

The soot inception stage comprises the pyrolysis of fuel that result in the formation of benzene rings which nucleate, and grow into solid soot primary particles. The threshold of soot formation (C/O_{crit}) depends on the fuel and oxidizer (which affect the differential diffusion), flame temperature (affected by heat losses), and ambient pressure [23]. Therefore, instabilities in the flame affect the structure of sooty flames through changes in the local composition and temperature. The process of soot production involves the formation of condensed-phase materials from gases, followed by mass and size growth through coalescence, coagulation and surface reactions, and finally by aggregation into fractal structures. The study of soot production and consumption is thus a complex task involving chemical kinetics, fluid mixing, heat and mass transfer, and phase transition [9].

The thermal decomposition of the unburnt mixture (Figure 1.3b), under suitable condi-

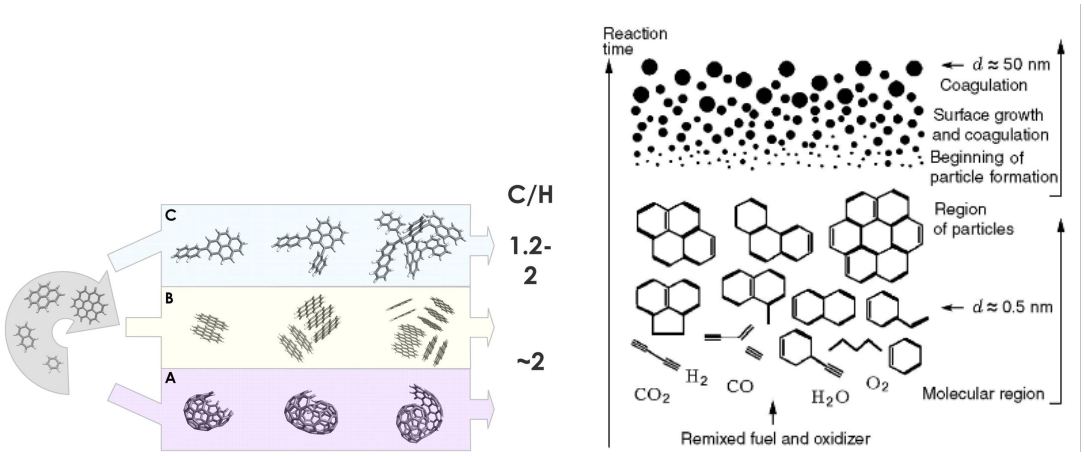

(a) Mechanism of PAH nucleation [24] (b) Soot evolution in the reaction zone [23]

Figure 1.3: Primary soot particle formation

tions, results in the formation of PAH [23, 25, 26], which are the precursors of soot particles [23, 24]. PAH formation has a strong dependence on the chemical kinetics. These PAHs are then transformed into solid particles via the nucleation process. The three mechanisms of soot nucleation are depicted in Figure 1.3a. Based on experimental evidence, Wang [24] concluded that dimerization (processes B and C) was the initial nucleation step resulting in the formation of particles in various size depending on their collision rates. This nucleation process is immediately followed by coagulation, when small particles (with higher velocity) collide with large particles (with high cross section), forming primary particles of 10-50 nm diameter. Meanwhile, surface reactions smooth the surface, producing nearly spherical particles. These primary-particle growth mechanisms then compete with the oxidation caused between oxygenated compounds and the surface of the soot particles, a way of consuming soot particles [10, 27]. Surface growth and conglomeration produces aggregates consisting of several primary particles that form arbitrary and complex fractal structures [23, 25]. Thus, the size of the soot particles and their morphology are a strong function of height above the burner. Furthermore, the chemical kinetics will contribute to these variation (size and morphology of the particles), along with concentration of soot particles produced (soot volume fraction).

1.2.3 Soot Restructuring

The complexity involved in the characterization of soot particles is exacerbated by the restructuring nature of carbonaceous soot (Figure 1.4 (a)) [28]. Restructuring of these monodisperse soot aggregates is known to occur in the presence of various combustion products that include water vapor [29–31], low vapor pressure products of aromatic hydrocarbon oxidation (OH-initiated oxidation of aromatic hydrocarbons) [31–33], sub-nanometer coatings of PAH [34], sulfuric acid [33, 35] , etc. The extent of restructuring depends on the production conditions of the particulate matter. Weingartner et. al., [29] characterized the hygroscopicity of diesel produced soot. Condensation of water vapor (from diesel combustion products) on the surface of soot showed growth in diesel soot particle diameter. Secondary organic aerosol, produced from OH-initiated oxidation of toluene and isoprene (aromatic HC), resulted in increase in density and significant decrease of dynamic shape factor of the cores [36]. Furthermore, exposure to glutaric acid leads to significant collapse of soot cores [37]. These intricate morphological characteristics are a strong function of the chemical composition of the fuel.

Recently, Baldelli et. al [38] noted the existence of atypical non-volatile particulate matter emissions in the exhaust of a marine engine fueled by diesel and a natural gas-diesel blended fuel mixture (Figure 1.4 (b)). Such particles were characterized as soot emissions and non soot particulate matter, and most of these features are consistent with the emissions from that of gasoline [38, 39]. The non-soot particulate emissions that were identified in the emissions from the same study are (i) spherical particles that contain Ca, P and O; (ii) mineral like polyhederal particles, that are surrounded by gray area that indicate the presence of volatile organics [39]; and (iii) fibres, which are identified to be carbon nanotubes or geoethites. Since these are not consistent with canonical soot behavior, it was hypothesized that these structures were most likely the result of partial combustion of lubrication oil (for spherical structures) and the lubrication additives (for ligament like structures).

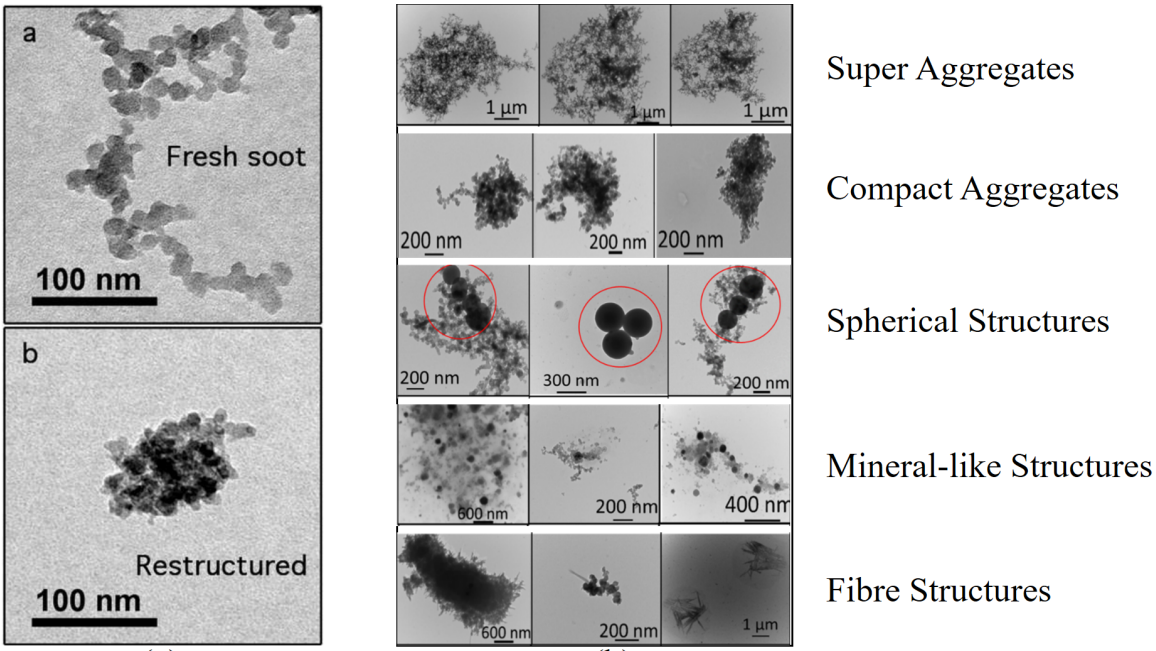

Figure 1.4: TEM images of soot morphology in diesel flames: (a) Restructuring of soot chain [28]; (b) Atypical aggregate characteristics [38]

Furthermore, this study also noted some key morphological characteristics of soot particles that include formation of (i) super aggregates - clusters of primary soot particles with radius of gyration in the order of few micrometers [40, 41]; (ii) unusually compact aggregates with few internal voids [42, 43], which may have high hygroscopicity affecting cloud formation [57]; and (iii) highly non-uniform aggregates with distinct groups of smaller and larger monomers were also observed.

It is of interest to perform non-intrusive diagnostics on flame generated particulate emissions of relevance in LPP combustors. However, the possibility of the presence of non-soot particles and restructuring nature of soot further complicate the interpretation of signals acquired from optical measurements. To overcome this issue, two types of diagnostic techniques are implemented. (i) A non-intrusive diagnostic technique that acquires data from the flame generated soot, which is calibrated and validated with the help of (ii) an in-situ sample extraction technique that simultaneously acquires physical soot specimen. The intrusive technique is also used to study the effect of (i) pressure, (ii) height above

the burner (indicative of the residence time of the combustion products), and (iii) equivalence ratio (concentration of species) on the soot production and its morphology in a rich premixed flame of a heavy (and complex) hydrocarbon fuel.

Thus, this thesis focuses on (i) the design and deployment of the intrusive diagnostic system that is capable of collecting extractive soot samples from an flame that is not only exhibiting inherent instabilities, but also capable of generating atypical particulate emissions; and (ii) analyzing the samples to provide the necessary structural and morphological characteristics of the acquired specimen. Finally, (iii) the line-of-sight integrated broadband flame intensity signal acquisition helps to understand the structure of this flame. Additionally, shared responsibility of performing the necessary optical diagnostics on a flame that exhibits spatio-temporal variations is also discussed in this thesis.

1.2.4 Optical Diagnostic Technique

Reliable in-situ non-intrusive techniques to study soot particles improve the understanding of formation, growth, aggregation, and the oxidation of soot particles in flames. While numerous optical techniques provide information on soot characteristics, including laser extinction, and laser scattering [6, 44] the focus here is on LII due to its potential for providing spatially and temporally resolved quantitative measurements for soot volume fractions and particle size [44]. More specifically, the focus is on 2D TiRe LII using nanosecond pulsed lasers for particle size measurement.

The fundamental concept of TiRe LII involves heating the soot particle using a high-fluence laser beam and quantifying particle size by analysing the temporal decay of the thermal emission (incandescence) from the soot (see Figure 1.5); the time taken for the soot particle to cool down is related to the size of the particle. However, the relationship between the incandescence decay and particle size is a complicated function of many physical processes, thus requiring a complicated and validated physical model.

The temperature history of particles are obtained by solving a set of coupled differential

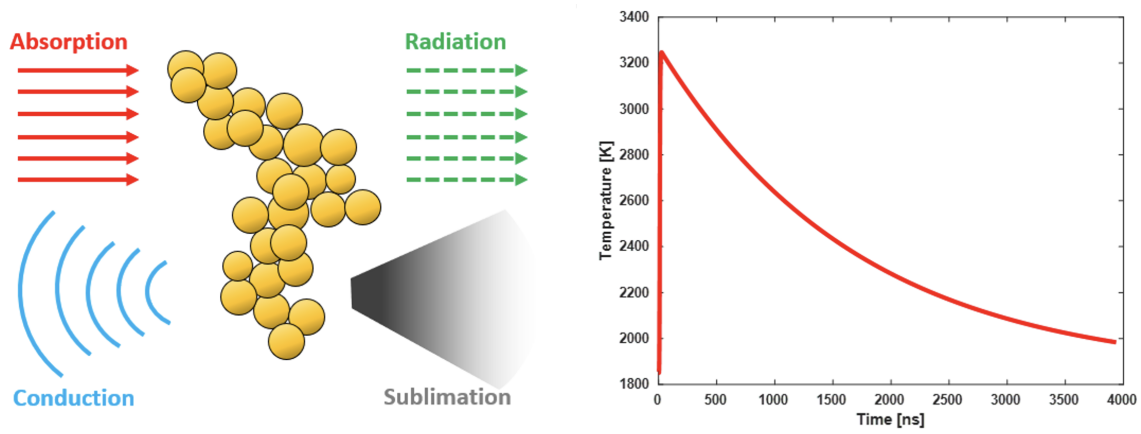

(a) (b)

Figure 1.5: Schematic of the TiRe LII model: (a) Modes on heat and mass transfer considered for the model; (b) Typical laser induced incandescence signal decay for flame generated soot.

mass and energy balance equations. This study uses the model developed by Liu et al. [45], which incorporates an improved model for heat conduction. The energy conservation equation is given by

$$\frac{dU_{Internal}}{dt} = \dot{Q}_{Absorption} - \dot{Q}_{Conduction} - \dot{Q}_{Radiation}, \tag{1.1}$$

the rate of change of internal energy is given by Equation 1.2; and the absorption & radiation heat transfer per unit time are given by Equation 1.3, & Equation 1.4 respectively

$$\frac{dU_{Internal}}{dt} = \frac{\pi}{6} d^3 N_p \rho_s c_s \frac{dT}{dt}, \tag{1.2}$$

$$\dot{Q}_{Absorption} = \frac{\pi^2 d^3 E(m) F_0 q(t) N_p}{\lambda}, \tag{1.3}$$

$$\dot{Q}_{Radiation} = N_p \int_0^\infty \frac{8\pi^3 c^2 h}{\lambda^6} \frac{d^3 E(m)}{exp(hc/k_B \lambda T) - 1} d\lambda = \frac{199\pi^3 d^3 (k_B T)^5 E(m) N_p}{h^4 c^3}, \tag{1.4}$$

where the Planck function is integrated over all wavelengths, and the Rayleigh approximation is used for the emissivity to obtain Equation 1.4. Here, d is the primary particle size of the soot particle, N_p is the number of primary particles per aggregate, ρ_s is the density of soot, c_s is the soot specific heat, $E(m)$ is refractive index function, F_0 is the laser

fluence, $q(t)$ is the laser temporal profile function, λ is the laser wavelength, and T is the temperature. The constants h, k_B, and c are the Planck constant, Boltzmann constant, and speed of light, respectively. For particle sizing, lower laser fluences are typically used to avoid sublimation of soot particles. Therefore, for low laser fluences, mass transfer is often neglected in the modeling.

The most complicated, and perhaps most important term, is the conduction heat transfer term in the model. The method used to calculate the heat conduction term depends on the conduction regime. At lower pressure conditions, the mean free path is greater than the particle size, so conduction is assumed to be in the free-molecular flow regime. At elevated pressure conditions, a transition regime conduction approximation is required. A technique used to approximate this is based on Fuchs method [46, 47], where a limiting sphere radius is defined. This radius is chosen such that inside the limiting sphere, free molecular regime conduction is assumed, and outside the sphere, calculations are based on continuum regime conduction. The continuum regime conduction equation is given by,

$$\dot{Q}_c = \alpha \pi {R_a}^2 \frac{p_g}{2} \sqrt{\frac{8 k_B T_\delta}{\pi m_g}} \frac{\gamma^* + 1}{\gamma^* - 1} \left(\frac{T}{T_\delta} - 1 \right), \tag{1.5}$$

where p_g is the ambient gas pressure, m_g is the mass of the gas molecule, T_δ is the limiting sphere temperature, and α is the soot particle thermal accommodation coefficient. R_a is the radius of an equivalent sphere calculated based on the aggregate project area given by [48],

$$R_a = \frac{1}{2} d \left(\frac{N_p}{f_a} \right)^{1/2\varepsilon_a}, \tag{1.6}$$

where the constants f_a and ε_a are given values 1.1 and 1.08 [49]. γ^* is an average specific heat ratio value given by,

$$\frac{1}{\gamma^* - 1} = \frac{1}{T - T_\delta} \int_{T_\delta}^{T} \frac{1}{\gamma - 1} \, dT. \tag{1.7}$$

Outside the limiting sphere, continuum regime conduction is given as,

$$\dot{Q}_c = 4\pi \left(\delta + R_a\right) \int_{T_g}^{T_\delta} k_g \, dT, \tag{1.8}$$

where δ is the boundary layer thickness and k_g is the conduction coefficient of the ambient gas. An example of the results from solving this set of energy and mass balance equations is depicted in Figure 1.5b.

One of the most challenging aspects of interpreting LII signals is that the soot is not uniform in its degree of maturity, size, morphology and optical properties. An increased amount of aggregated cluster leads to reduction in the heat conduction because the exposed surface area for heat transfer in the penultimate primary particles is diminished, when compared to the case where the same particles are isolated. This is known as the shielding effect and makes the obtained time constants imprecise. Therefore, the resultant particle size deduced from the TiRe-LII model needs to be calibrated. This can be achieved with the help of data from directly sampling the soot in the flame at the location where the optical measurements are made.

1.2.5 Intrusive Diagnostic Technique

Extractive soot sampling from laminar flames may be conducted by leveraging thermophoresis, which is the movement of suspended particles through a fluid under the influence of an applied thermal gradient. This phenomenon enhances particle deposition onto cooled surfaces. The thermophoretic force is only significant at relatively low fluid velocities [50]. Thermophoretic soot sampling is based on the fact that soot deposition rates on cold targets immersed in laminar flames are dominated by particle thermophoresis. While the idea of sampling soot with thermophoresis was postulated by Eisner et al. [51] in 1985, the first successful system was designed by Dobbins et al. [7] in 1987. A sampling time of 40 ms was sufficient for getting satisfactory distribution of soot samples on the sampling grids in

a diffusion flame burning ethylene. This study also reported reduced primary particle size and state of agglomeration on oxygen rich side, and fuel rich side of the diffusion flame. Since then, thermophoretic soot sampling followed by Transmission Electron Microscope (TEM) imaging has been one of the most common techniques used to collect soot samples in flames [7, 8, 12, 13, 51–57].

Köylü et al. [52] designed a thermophoretic sampling particle diagnostic (TPSD) to extract samples in diffusion flame burning ethylene, and compared the results with laser extinction measurements. This study concluded that the presence of translucent soot precursors, which do not absorb as much visible light as mature particles, was the reason for a large variation between the data of comparison. Similarly, the complexities associated with the unknown optical (refractive index) and morphological properties of flame generated soot was also a contributor for the disparities in the results between light scattering based size determination in laminar premixed methane-oxygen flames [58]. This study also evaluated the effect of 3D to 2D projection of aggregates (for planar optical measurements, and electron-microscope imaging for soot chains).

As discussed earlier in the section, the structure and morphology of soot particle is affected by type of fuel, sampling location (height above the burner), pressure, temperature, and presence of PAH, water vapor, sulfuric acid, etc. The direct effect of this is the formation of enormous structures for complex fuels like diesel, kerosene etc. Therefore, the insensitivity of the efficiency of depostion to the size and morphology of the soot chains is required to extract flame generated soot samples. Studies by Resner et. al. [55] concluded that the thermophoretic deposition can adequately extract soot particles of varying size and structure. Messerer et. al. [53] also observed a satisfactory thermophoretic depostion of 30-300 nm sized particles in diesel flames. Furthermore, it was concluded that the observed deposition efficiencies exhibit no decrease with increasing aerosol particle size. These observations are in agreement with a recent theoretical study by Rosner and Khalil [54] on the effect of reduced thermal conductivity on the thermophoretic coefficient of agglomerate

particles. Therefore, it is concluded that the thermophoretic sampling is an ideal choice for extracting nvPM samples in flames involving complex chemistry of fuels.

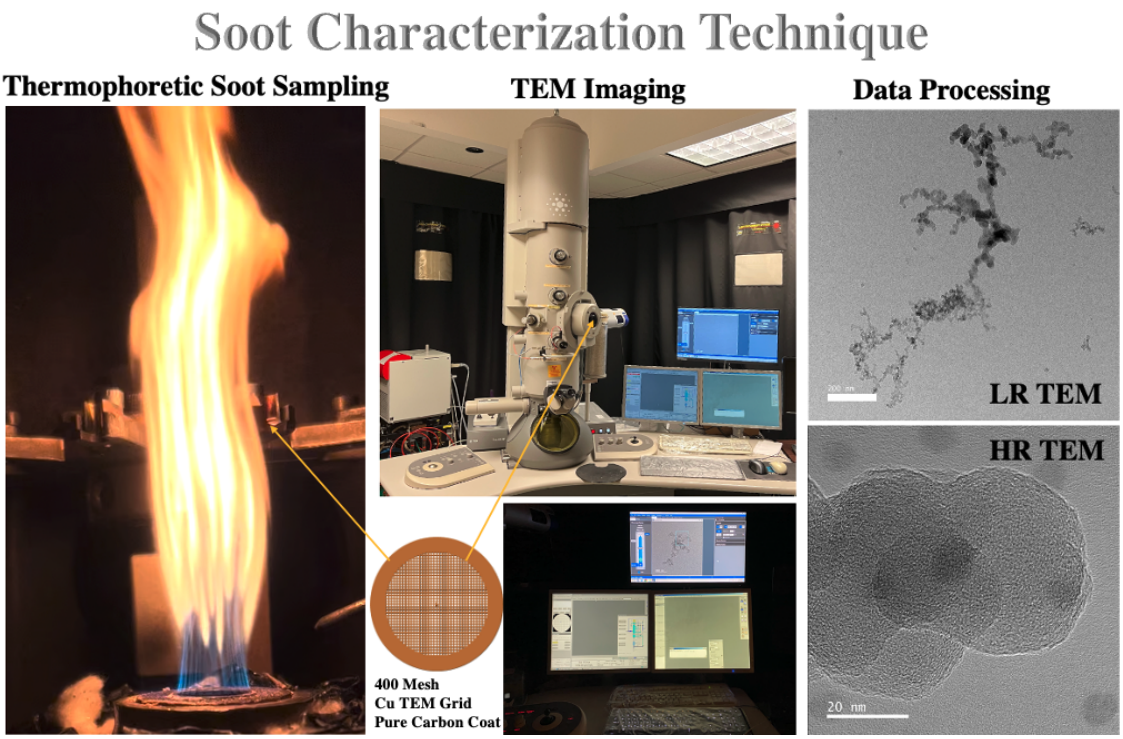

Figure 1.6: In-situ extractive sampling methodology.

The main steps in thermophoretic soot sampling are depicted in Figure 1.6, which are from the present work. TEM grids (typically copper grids with protective coating) are used to sample the soot in the flame. These grids are rotated into and out of the flame using a stepper motor. The two key factors that influence the amount of soot particle deposition are the transit time and the grid exposure time. The transit times into and out-of the flame are determined by the RPM of the motor rotation, whereas the exposure time is the duration over which the grid is held static in the flame. If the grid sits in the flame for a very short sampling time (transit + exposure time), then insufficient soot particles are collected for subsequent analysis. On the other hand, longer sampling times can deposit particles on top of each other, corrupting the samples, or even melt the TEM grid.

Botero et al. [8] and Vargas et al. [12, 56] investigated the dependence of sample quality on sampling times by varying these parameters and estimated the best suited values

based on multiple trials. Their investigations showed that a sampling time in the range of 35-50 milliseconds gave the best particle distribution in the TEM grid for diffusion flames. Similar studies have been performed for the flame under investigation, and the details of operation can be found in chapter 2.

Primary soot particles typically are 10-50 nm in diameter. Measuring these length scales requires electron- or atomic force microscopy, depending on the properties of interest. Here, primary soot particle size and aggregate morphology are the focus, which can be determined by TEM. Low-Resolution Transmission Electron Microscopy (LRTEM) is sufficient to determine morphological information, including primary particle diameter, aggregate projected area and radius of gyration; High-Resolution Transmission Electron Microscopy (HRTEM) is typically required to obtain qualitative information on the nanostructure of the particles [8].

TEM images must be post processed and analyzed to determine the desired soot properties. Typically, the soot particles are observed to be an arbitrary aerodynamically-sheared-ellipsoid. The primary soot particle size (or primary particle diameter, d) of a single particle is defined as the longest length of that particle [7, 12, 56]. The compositions and morphology of these particles depend on the type of fuel, flame structure, ambient pressure and temperature, and the location of sampling in the flame. This dependence is investigated in this research.

CHAPTER 2
DESIGN AND DEPLOYMENT OF THE EXPERIMENTAL SETUP

2.1 Introduction

This chapter describes the Laminar Flame Burner (LFB), the extractive soot sampler and the associated optical diagnostic setups that are used to accomplish this investigation. Description of the commissioned test rig are provided in section 2.2, along with the details of necessary mass flow rate metering equipment. The modifications made to the test section to perform optical diagnostic techniques on the flame of interest is also elaborated. While the experimental setup for 2D TiRe LII is discussed briefly in section 2.3, the design of the thermophoretic soot sampler (TSS) system is elaborated in section 2.4. Details of assembling the TSS system into the LFB is described in section 2.5, along with its operation. This system was configured to extract soot samples from various locations (axial and azimuthal) in the flame. The steps involved in deploying the soot sampling system, details of its operation, and the test matrix is included in section 2.6. The description of the facility used, and the imaging techniques employed for visualizing the data is elaborated section 2.7. The data post-processing procedures, and subsequent statistical data processing is included in section 2.8. Finally, section 2.9 contains the limitations of the experimental setup.

2.2 Laminar Flame Burner

The test rig for conducting the experiments is set up in RM122 at the Ben T. Zinn combustion laboratory. The existing burner [59–63] is reconfigured (see Figure 2.1) to burn liquid jet-A (fuel) at elevated pressures, using heated air as oxidizer. The rich, preheated, prevaporized, premixed, axisymmetric, laminar flame from the burner is surrounded by nitrogen co-flow. The main flame is stabilized using a stoichiometric methane-air pilot flame

downstream of a sintered plate that is coannular with the main nozzle. The pilot flame is ignited using a 11 kV spark plug ignitor. The burner is housed inside the pressurization chamber where the ambient pressure of the flame is controlled with the help of a custom designed high temperature back pressure regulator (Equilibar OEM GSDH/HT series) that can operate upto a mass flow rate, temperature, and pressure of 15g/sec, 800K and 12 bar respectively.

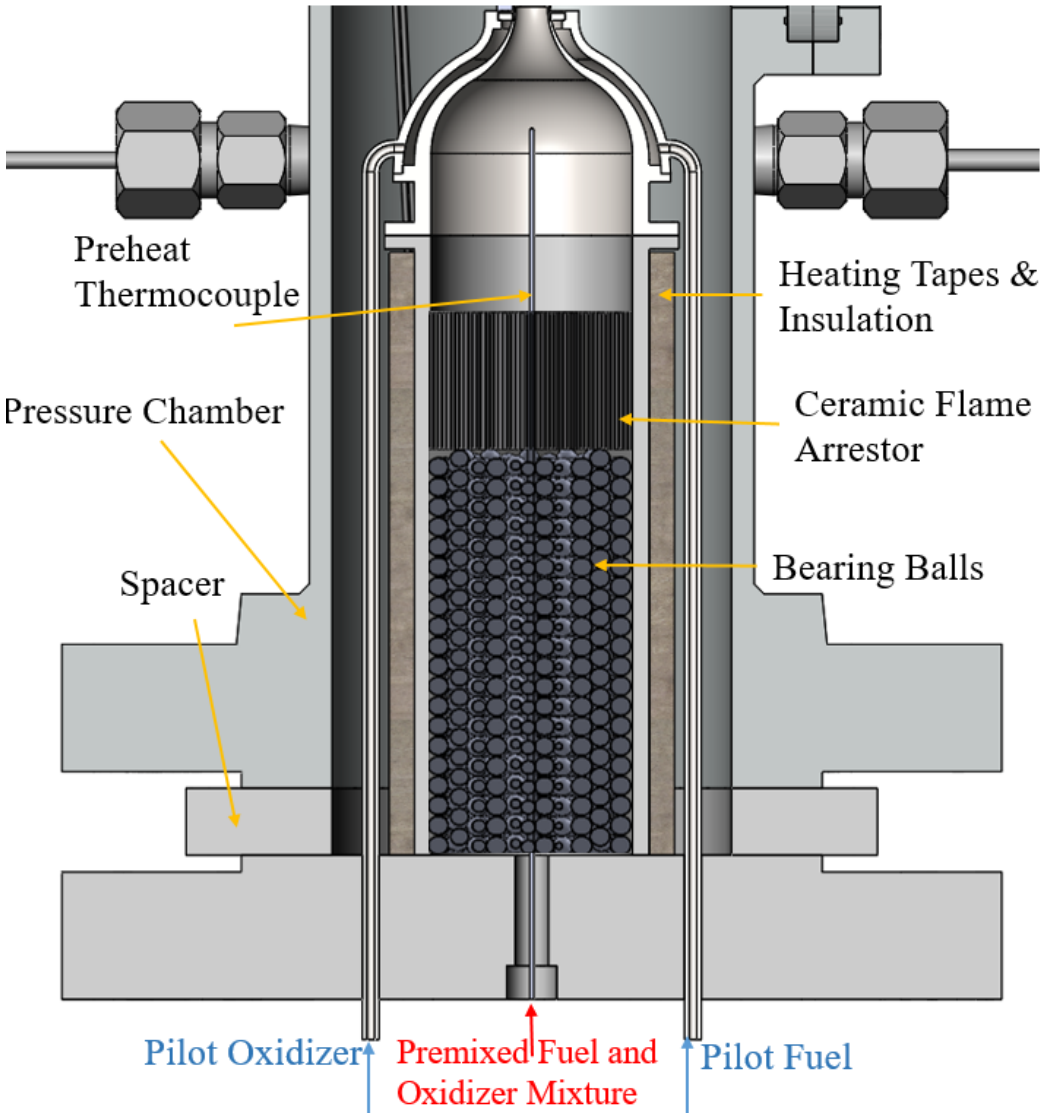

Figure 2.1: Burner nozzle assembly

The specifications of the components for flow metering and control set the operational

limits of the burner. These components (critical orifices, rotometer, etc.) are sized to operate at a peak equivalence ratio of 1.5 at 8 bar which yields a flame observable though the optically accessible windows of the pressure chamber. Furthermore, the base plate of the burner nozzle assembly is also equipped with a provision for spacers (Figure 2.1) that help with the optical (and mechanical) access for the sooty region of the flame.

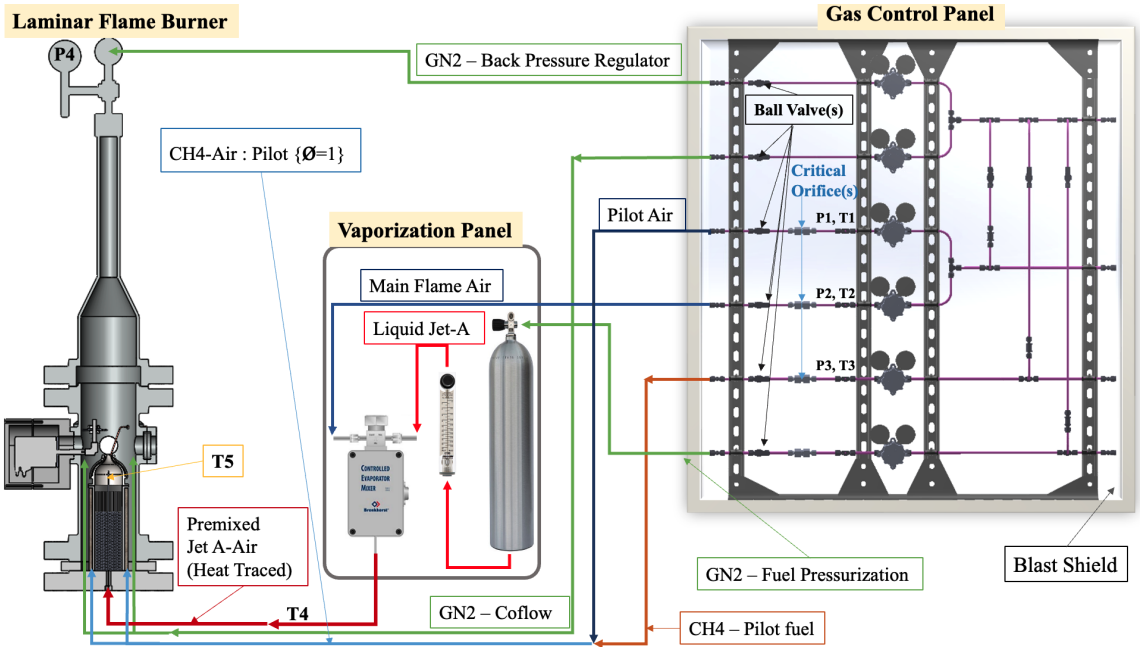

Figure 2.2: Schematic of the flow metering and control setup.

The gas control panel (Figure 2.2) allows accurate metering of (i) gaseous nitrogen for back-pressure regulator, co-flow and fuel-tank pressurization; (ii) bottled compressed air; and (iii) bottled compressed methane. The vaporization panel (Figure 2.2), on the other hand, facilitates (1) precise control of liquid fuel flow rate; and (2) atomization & vaporization of the fuel. This panel comprises a fuel tank that is pressurized with gaseous nitrogen; a rotometer that is calibrated at the tested setpoints; and finally, a commercial evaporator (Bronkhorst Controlled Evaporator Mixer Type W-303A-222-K), that atomizes the fuel with the help of heated air to produce a homogeneous gaseous mixture that is heated to 475 K at its exit. To ensure good mixing, the preheated premixture is allowed to flow through 8 feet of 1/4" tubing. Furthermore, these tubing are insulated and heat traced,

to avoid fuel condensation on the tubing walls. This is achieved with the help of electrical heating tapes that are controlled by a 600 W, 5A Extech precision temperature controller. The burner inlet temperature is monitored to determine the set point for this controller.

The preheat temperatures inside the burner (Figure 2.1) is controlled by a 600 W, 15A (high-current) Briskheat precision controller (SDXKA-Digital PID contoller) with the temperature feedback from the thermocouple carefully positioned near the tip of the nozzle. The entry gas flow path in the burner-nozzle assembly is also filled with steel bearing balls to ensure uniform temperature distribution, enhanced (thorough) mixing, as well as serve as a secondary flash back arrestor. The burner is also equipped with a ceramic quenching mesh as the primary flash back arrestor.

Two of the three flame access ports in the pressurization chamber are equipped with high transmission optical windows that enable LII laser transmission, and signal collection. The third access is used used to mount the chamber extension for housing the motor for TSS system. The following sections elaborate diagnostic setup used and the associated the experimental procedures of the study.

2.3 Laser Induced Incandescence

Single camera, single laser shot 2D TiRe LII [64] is performed to analyze nvPM along the centerline of the main flames. Figure 2.3 is the schematic of the optical train used to create the laser sheet with a top-hat intensity profile. A 10 Hz, 1064 nm laser (Quanta-Ray PRO-350) is used to heat nvPM in the flame and incandescence decay is obtained along a 30 mm long, 2 mm-thick laser sheet at 65 mJ/cm^2 fluence. The decay is captured at 10 MHz using an ultra-high-speed camera (Shimadzu HPV-X2, 50 ns exposure) through an objective lens (85 mm, f/# = 1.8) and a bandpass filter (640 ± 75 nm) to block chemiluminescence. It needs to be noted that LII signals were simulteneously acquired with the extractive soot sampler. Therefore, a 1064 nm mirror is used to block the reflected and scattered laser beam from the installed soot sampler.

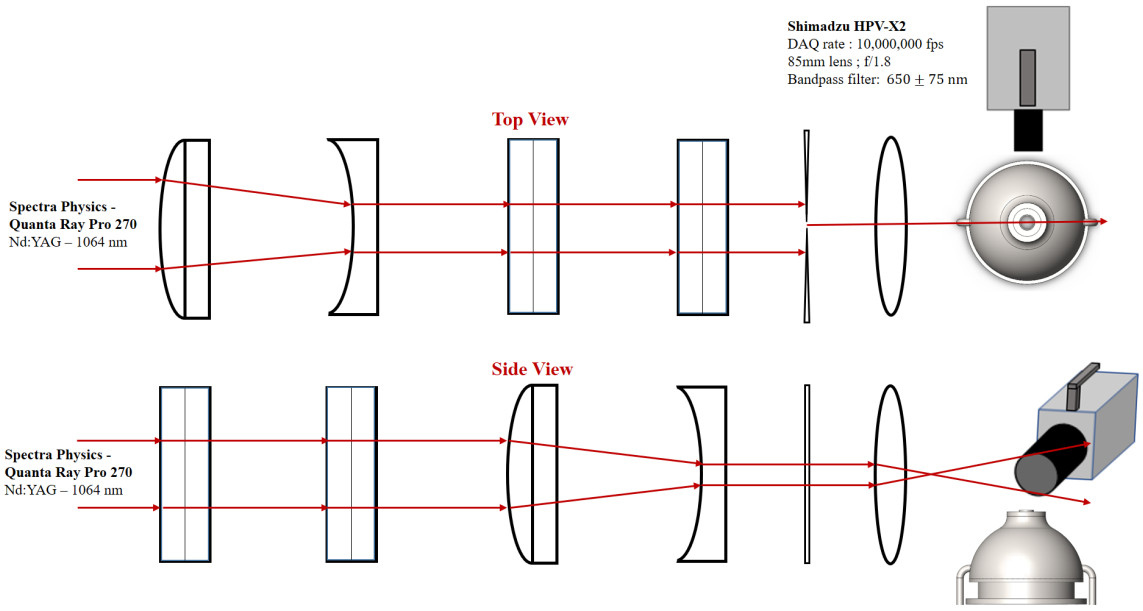

Figure 2.3: Optical diagnostic setup for LII.

The LII study is the primary responsibility of another student, so it is not discussed in detail in this report. However, it can be useful to compare the the time constant distribution obtained form the LII signal decay to that of the the particle size distribution from the extractive soot sampler data. It should also be noted that the plane of sampling for the soot sampler is normal to that of the LII data acquisition. Therefore, the distribution of time constant should be obtained from an ensemble of decay signals obtained at a fixed location above the burner.

2.4 Thermophoretic Soot Sampler

The main focus of this thesis is the design and operation of the Thermophoretic Soot Sampling (TSS) system; and subsequent analysis of the collected soot samples. The TSS system consists of the following components.

1. ***Sampler Assembly (SA)*** that comprises the sampling disc base plate, TEM grid support, a shaft collar and base plate support disc (Figure 2.4).

2. ***Drive Train Assembly*** that comprises of the shaft extension, compact miter gearbox,

anchor, hexagonal shaft, an additional shaft collar (Figure 2.5); and

3. ***Chamber Extension*** housing for the motor and the associated wire seals (Figure 2.5), drive train assembly and the sampler assembly to facilitate operation in a pressurized environment.

4. ***Motor Drive System*** that comprises of a stepper motor (Figure 2.5), and its control system.

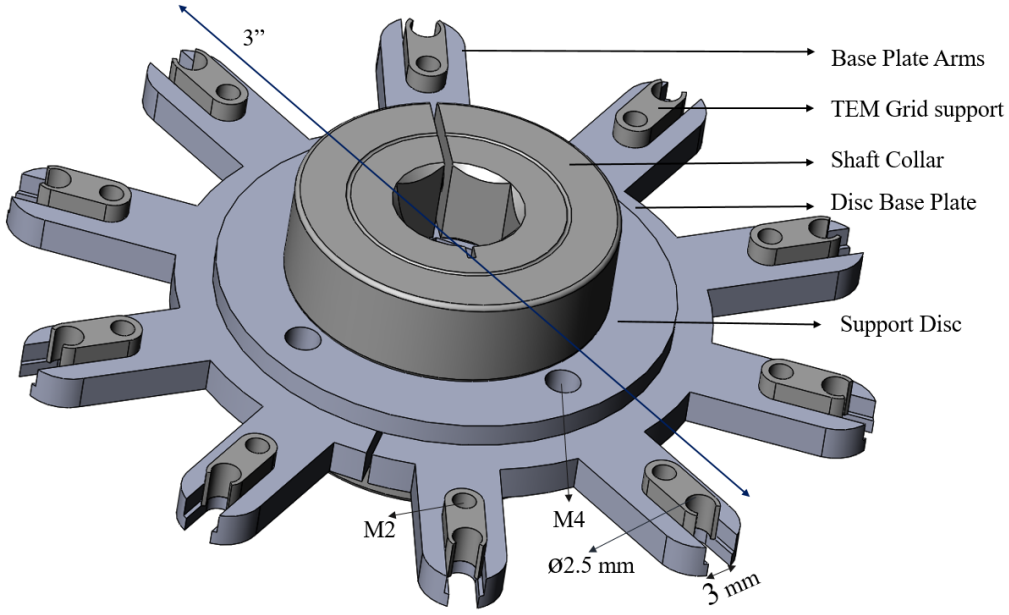

Figure 2.4: Sampler assembly.

Based on literature, TEM grids made out of copper are the ideal choice for sampling soot in flames [65–67]. Considering the operational environment of this sampling grid, a 400-mesh copper grid coated with pure-carbon nanofilm is used. The sampling disc base plate (Figure 2.4) is designed to house 10 such uniformly spaced TEM grids. Each of these arms houses one TEM grid that is held in place by a precisely designed TEM grid support. Sufficient care is taken for sizing the arms and its grid support to secure the grids without causing any damage to the film on the grid. A modular design approach is taken to fabricate the base plate in two identical halves, allowing easy installation and faster grid

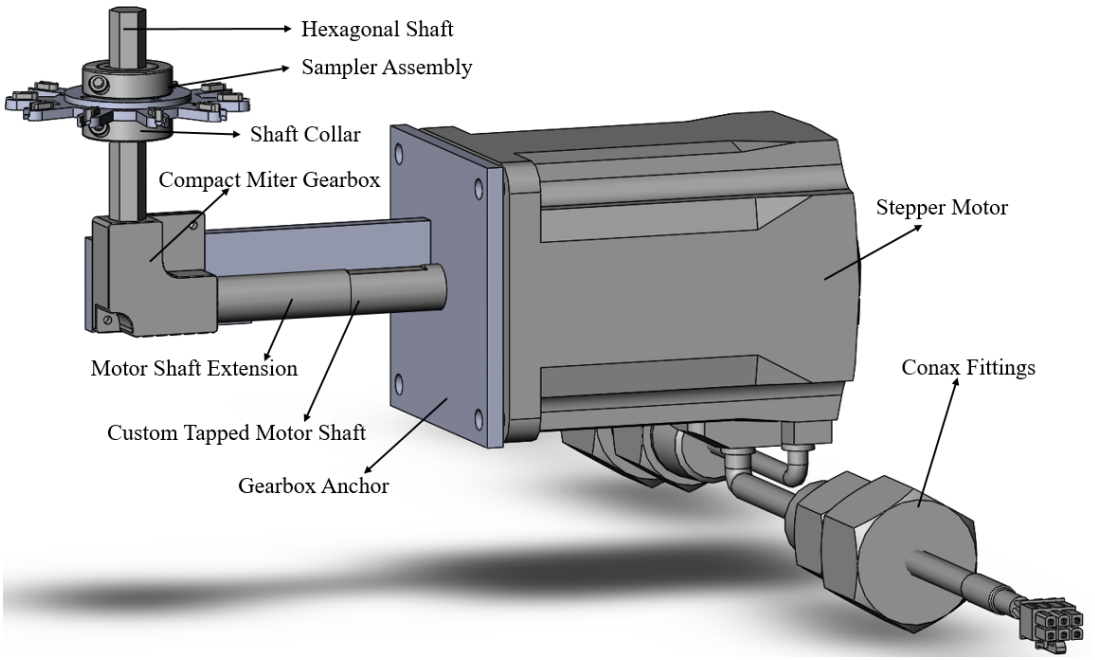

Figure 2.5: Drive train assembly with the AC stepper motor.

swap. These half plates are held in position by a custom designed support disc that is welded to an altered shaft collar to secure the position of the SA on a hexagonal shaft. The engineering drawings for the SA can be found in Appendix B.

It was decided to install the TSS system through one of the window ports. This configuration, along with the available space in the pressurization chamber-burner assembly, necessitates the need for a miniature miter gear box that is secured in position by a custom designed anchor to fix the axis of rotation. The drive train assembly (Figure 2.5) is carefully designed around this gearbox-anchor configuration to transfer the rotational motion from stepper motor to the hexagonal shaft. This required an extension of the motor shaft, which is achieved by drilling and tapping the cross section of the motor shaft through its center line, and securing the extension with a thread locker. Furthermore, the hexagonal shaft has an additional shaft collar that allows repetition of the height at which soot samples are extracted from the flame.

The moving components of the TSS system in the motor make it challenging to place the motor external the pressure vessel, with the drive shaft operating through a pressure

seal. Instead, it was decided to build an extension to the pressurization chamber around the stepper motor (Figure 2.6). To facilitate motor installation (or replacement), precision mounting, and easy alterations. This extension is fabricated in two halves secured by bolts. The front half of the chamber has a geometry that mimics the male version of the window-mounting pattern on the pressure vessel, and it is attached to the rear half that houses the motor cables and required grounding terminals. The pressure seals in the metallic interfaces and electrical wires (with varying cross sections) is achieved with the help of grafoil gaskets and split gland conax fittings (in the rear half of the chamber) respectively.

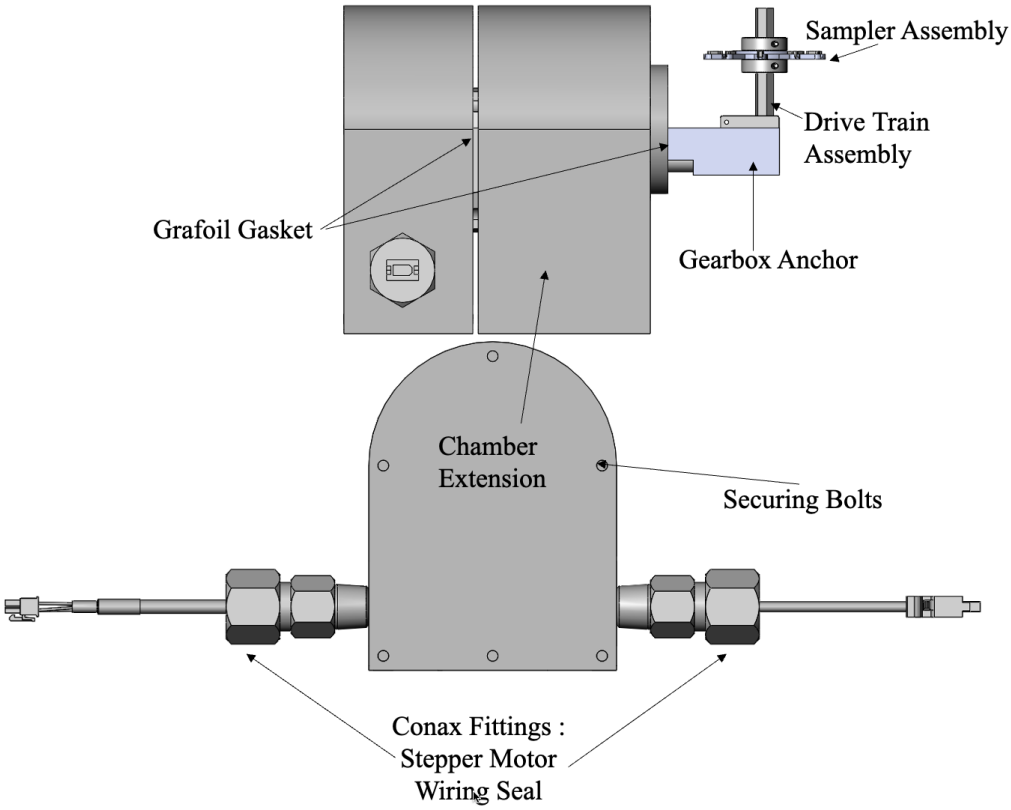

Figure 2.6: Extension to the pressurization chamber - TSS system assembly.

Figure 2.7 is the schematic of the control system circuit for the motor drive system (MDS). This system consists of a single phase AC stepper motor (Oriental Motors AZM911 AC) and a programmable drive (AlphaStep AZ Series closed loop driver) that can carry out the necessary spatial and temporal steps. The motor has a resolution of 0.36 degree per step and 3.5 N-m torque at 400 rpm. The 120V AC power source is connected to the driver

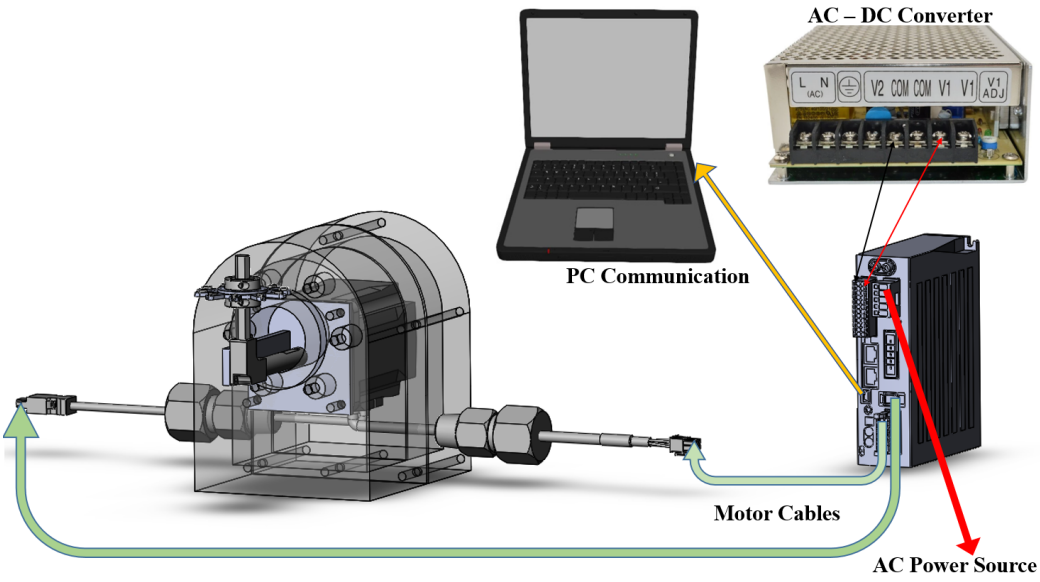

Figure 2.7: Schematic of the control system setup.

that powers the motor; and controls its angular position. A USB connector is used for communicating with the stepper driver. Sufficient care is taken to (i) maintain the motor under the allowable max operation temperature by operating it at 10 percent of its peak operational capacity; and (ii) electrically isolate the system from the 11 kV spark plug discharge.

2.5 Installation and Operation of the TSS

Although the SA is designed to have the TEM grids replaced through the window ports, the Height Above the Burner (HAB) at which soot was produced did not allow for this easy grid replacement. Additionally, considering the fragile nature of the TEM grids and the dimensions of the TEM grid support in the SA, it is deemed necessary to replace the TEM grids by disassembling the exhaust flange of the burner. The SA is then dismounted from the drive train, and the TEM grids are replaced. Thus there are two main sub-assemblies: (1) permanently installed TSS-LFB assembly (as described in Appendix A), that consists of the chamber extension, drive train, and the stepper motor; with (2) the frequently re-assembled SA (see Figure 2.8), which is mounted upon installing the hexagonal shaft. In

order to (i) minimize the amount of overhauls required to replace new TEM grids; and (ii) obtain sufficient soot samples from the flame, the sampler disc was operated to collect samples from two different flame conditions for each run.

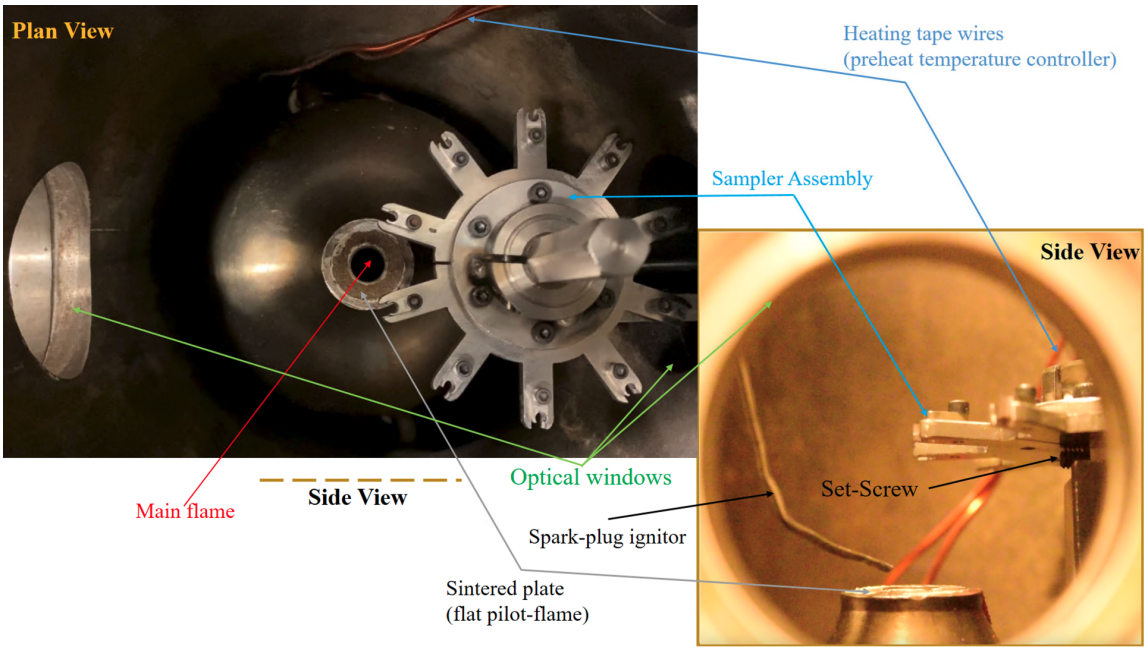

Figure 2.8: Assembled TSS system.

Initially, the TSS system is assembled on the LFB without the hexagonal shaft. The hexagonal shaft is then installed from the top, which is accessed by disassembling the exhaust flange, and secured tightly in its position by a setscrew as seen in the side view of Figure 2.8. Upon installing the hexagonal shaft, an additional shaft collar is mounted to facilitate repeatability for sampling HAB; followed by the SA installation. Figure 2.8 shows the ultimate physical assembly after installation, without the additional shaft collar that sits underneath the SA. This setup is used to program the stepper motor controller with the help of MEXE02 software, that is configured to take various inputs, most important of these are (i) angular position (degrees), (ii) delay (ms), and (iii) RPM (deg/sec).

Figure 2.9 shows the control system software (MEXE02) window, which is used to control and monitor the motor operation. The temperature of the stepper motor is monitored through the status monitor window (Figure 2.9), while operating the stepper motor. Various

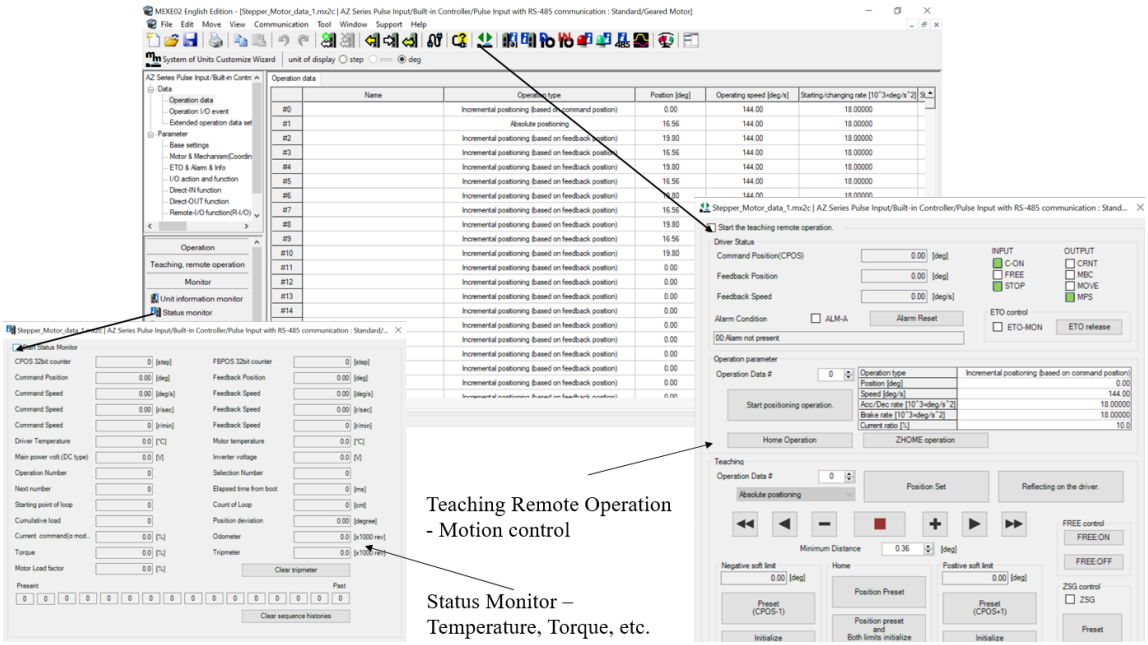

Figure 2.9: Stepper driver control system & monitor - MEXE02 Software.

parameters of motor control like (i) position; (iii) RPM; (iv) acceleration (and deceleration); (v) % of current drawn during operation; and the (vi) delay; are controlled through the programmed remote teaching operation. Furthermore, since the time taken to obtain the flame at different equivalence ratios is unknown, two programs are created (and written to the driver) for extracting samples at different flame conditions for each rotation of the soot sampler. While the first program controls the motor movement for arm #1 - #5, the second program that controls the rest of the arms, (#6 - #10), by referencing the position of sampling arm #5, that is obtained from the first sampling operation.

2.6 Design of Experiments

This section delineates the process involved in the deployment of TSS based on preliminary results, along with the test matrix. The choice of operational parameters and the tests conducted to determine these are elaborated in subsection 2.6.1; and subsection 2.6.2 encompasses the details of the test conditions at which the physical soot samples were extracted.

2.6.1 Operational Parameters

The two major parameters that need to be determined are (i) location of the sampling: planar (azimuthal and radial) locations, and height above the burner; and (ii) sampling duration. While the former is dependent on the physical dimension of the sampling arm and the position of stepper motor; the sampling time has a coupled dependency of RPM of the stepper motor, and its delay time at the specified location. These parameters are dependent on various aspects of (1) flame, that include its structure, amount of soot produced, and its spatio-temporal variations; and (2) soot sampler, which include amount of soot deposited (via thermophoresis), motor-gearbox induced backlash and oscillations, and the vibrations induced by the stepper motor. The effect of each of these characteristics, and procedures employed for determining its respective performance metrics is discussed in this subsection.

Sampling Location

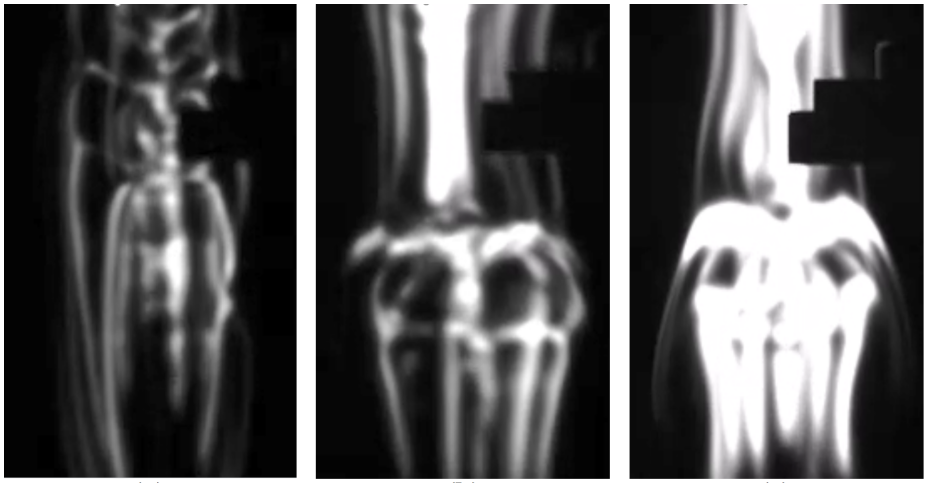

Figure 2.10: Streaky nature of sooty jet-A flame at 20 psig: (a) ϕ =1.96;(b) ϕ =2.19;(c) ϕ =3.2.

While the minimum sampling HAB is taken as the least height at which TiRe LII signals were detected, the maximum height was restricted to the location just above the field of

view of the Shimadzu camera (LII signal imaging system). The sampling HAB is adjusted by the anchoring the additional shaft collar, mentioned in section 2.5, on the hexagonal shaft. Furthermore, upon successful deployment of the LFB test rig, a unique structure of flame generated soot was observed. Figure 2.10 shows the sooty region of the flame for varying equivalence ratios, which was found to exhibit spatio-temporal oscillations. Hence, the radial and azimuthal sampling locations should be capable of extracting soot samples from multiple locations in the sooty region of the flame.

As noted in section 2.5, it was decided to extract soot from two different flame conditions for each rotation of the soot sampler. However, during the operation of LFB, the secondary reaction zone formed by pyrolysis of unburnt fuel, as shown in Figure 2.11, was observed while increasing the equivalence ratio from a lean mixture. This secondary flame is broad enough to come directly in contact with the sampling arms, which in-turn heats the SA and thereby increases temperature of the TEM grids through heat conduction. While this may affect the amount of samples deposited thermophoretically through reduced thermal gradient, the sampling time can be adjusted accordingly to obtain sufficient samples without defacing the TEM grids. The procedure for determing the sampling duration is elaborated in subsubsection 2.6.1.

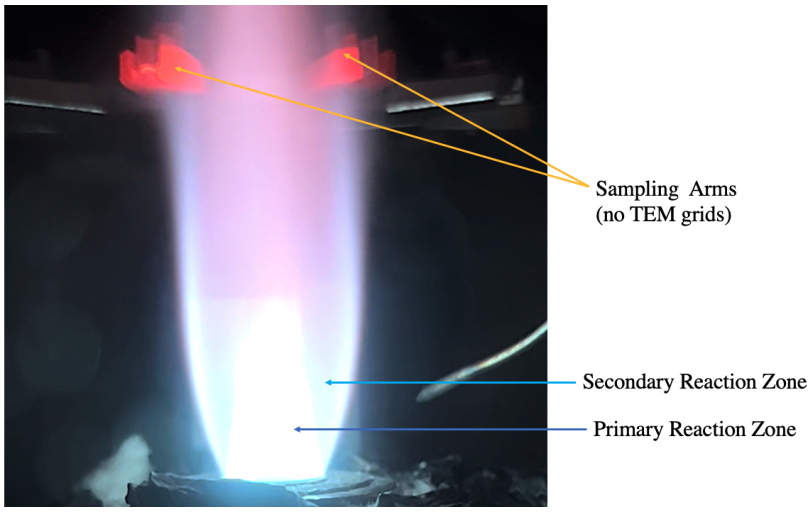

Figure 2.11: Secondary reaction zone burning the sampling arms.

Furthermore, this issue necessitated the need to ignore 2 sampling arms per equivalence ratio, which gives 3 reliable sample extraction per test condition. Considering all the above-mentioned contingencies with the installed soot sampler and the properties of the flame, it is necessary to sample at 3 different planar locations in the flame. The schematic of the sampling location for this three TEM grid system is represented in Figure 2.12a, and Figure 2.12b is the image of the deployed system in its steady state, following the oscillatory effect on sampling location due to the gearbox backlash-induced motion. It has to be noted that the sampling (arms) are sequenced as depicted in this figure, to ensure that strictly these TEM grids extract soot samples from the flame per test equivalence ratio.

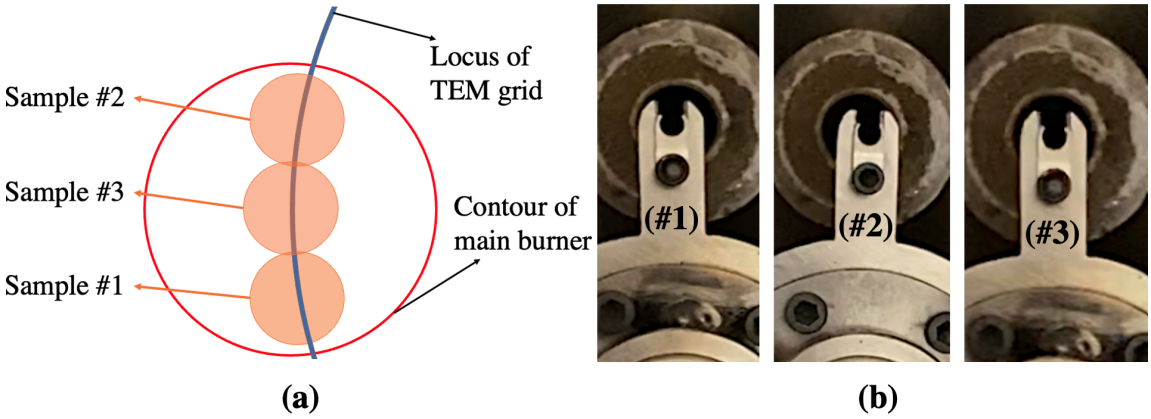

Figure 2.12: Azimuthal sampling location: (a) Schematic representation; (b) Deployed system.

Sampling Duration

Contingencies on the sampling time include obtaining samples for a duration long enough to (i) obtain sufficient particle deposition on the TEM grid, and (ii) account for unsteadiness in the flame; while not sublimating the carbon-nanofilm, where the samples are deposited, and (or) melting the TEM grid. The sampling duration is controlled jointly by delay time at the sampling location, and RPM of the stepper motor. The combined effect of RPM of the motor and the physical dimension of the sampler, on the other hand, impacts the extent of intrusion on the flame.

Physically smaller system with the high RPM for motion has the least intrusion, which is desired. The best way to minimize the intrusive nature is achieved by (i) designing the sampler to support the TEM grid very close to its bottom face; and (ii) waiting for sufficiently long time prior to extracting samples on the next arm. To reduce the number of independent control variables, the motor was operated at a fixed speed of 144 deg/sec (24 RPM), based on the data obtained from literature [56]. Furthermore, to further dampen the backlash induced oscillations and reduce the load on gear teeth, the acceleration (and deceleration) of the motor was maintained low at 18 x 10^3 deg/sec^2. Thus, the delay of the motor is the only independent variable to be determined to obtain the soot samples.

The sampling duration was then obtained by fixing the location of sampling and motion of the motor that include its RPM, acceleration, etc., for varying delay time in each arm; to extract samples on their respective TEM grids in a sooty flame at 20 psig. The delay time for these runs was varied from 35 ms in the first arm, and in subsequent increments of 10 ms for succeeding arms. These samples were then observed through the TEM, to see if sufficient samples have been collected. By the end of these tests, it was found that the delay time between 115ms and 145ms yielded satisfactory sample distribution on the TEM grid. Therefore, a constant motor delay time of **125 ms** were taken as the sampling duration for all the physical soot sample extractions between 0 - 40 psig. The significant deviation from the sampling time available in literature can be attributed to the spatio-temporally varying streaky nature of the sooty flame. The significantly long exposure time is expected to affect the nanostructures of deposited particles due to its longer exposure to combustion products.

Figure 2.13 is the series of images recorded for one sampling arm extracting soot in a premixed flame at atmospheric pressure. The operation has 3 phases: (1) sampler rest phase (1.5 seconds long), where the consecutive arms of the soot sampler are away from the flame; (2) transit in (and out) phase where the sampler moves in (and out) of the flame; and (3) sampling phase (125 ms), as deduced from the preliminary data acquisition. While the series of images in row#1 and row#3 depict the rest and transit phase of the soot sampler,

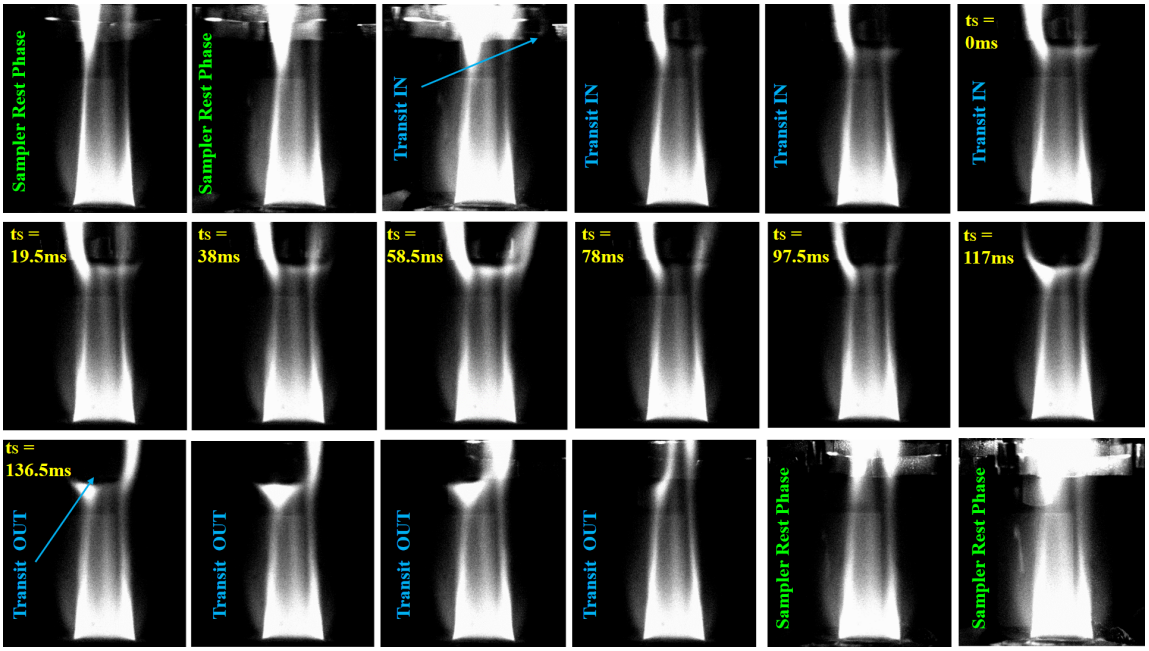

Figure 2.13: Operation of the soot sampler : Resting - transit in phase (row #1); Sampling phase (row #2); Transit out - resting phase (row #3).

row #2 shows the sampling operation.

2.6.2 Test Matrix

This subsection specifies the test matrix that was employed to study the effect of soot particle size on (i) equivalence ratio, (ii) height above the burner, and (iii) pressure. The experiments were conducted for 3 sampling HAB: 35 mm, 40 mm and 45 mm. Each of the sampling heights had tests performed at 3 pressures: 0 psig (atmospheric), 20 psig (1.4 bar), and 40 psig (2.75 bar); with each of these pressures having 4 test equivalence ratios that vary between (i) 1.8 and 3.5 at 0 psig; (ii) 1.9 and 3.25 at 20 psig; and (iii) 1.6 and 2.15 at 40 psig, respectively. This gives 36 test conditions overall. However, the data collected at atmospheric pressure did not yield sufficient samples. This can be attributed to (i) low sampling heights for the tested equivalence ratios, and (ii) the instabilities that produce low frequency spatial oscillations, which require larger sampling duration that was long enough to damage the TEM grids. Therefore, the data presented are for samples extracted at elevated pressures (20 and 40 psig), that yields 24 test data points. Finally,

the fuel rotometer is calibrated at the setpoint of the tested flame conditions to obtain their respective equivalence ratio.

2.7 Data Visualization

This section provides the description of imaging systems and their respective software employed for performing each of the mentioned diagnostics on the flame.

2.7.1 Transmission Electron Microscopy

Based on the quality of the images obtained during the preliminary testing, it was determined that the Tecnai G2 F30 S-TWIN 300 kV / FEG transmission electron microscope facility was best suited to provide the necessary details of soot particles that are useful in this investigation. Use of this TEM facility involved the alignment of electron gun, condenser and objective lenses at a electron beam spot size of 3. Sufficient care was taken to avoid stigmation error by monitoring the FFT of the live image. Operation of this microscope is controlled by interfacing the following software provided by Tecnai-FEI in unison: (i) TEM user interface - which control the electron beam and the holder position; (ii) Filter Control; (iii) Digital Micrograph - to interface Gatan microscopy suite (GMS) with TEM control software; and (iv) TEM images and analysis (TIA).

The focus of the acquired images is achieved by changing the (i) z-location of the TEM grids for coarser adjustments; and (ii) beam focus (along with its step width) for finer adjustments. The perfectly focused image produces the least contrast between the particle and the background, which is not ideal for determining the size and structure of the particles. Therefore, the images are slightly defocused to produce the best contrast for visualizing the edges (and structure) of the specimen [68]. The magnitude of underfocus plays a role in determining the pixel width of the border. So, the variation in finer focus was adjusted to the least step size, beyond which the adjustment provided no variations. This was sufficient to provide the details of the structure of the soot particles required

for processing the obtained data. This TEM facility was equipped with a high-resolution camera (Gatan OneView) operated to provide images at 4K resolution. The choice of magnification depends on the morphological characteristics (size of the soot chains) of the extracted samples. The exposure time of the imaging system was constant at 0.5s. Furthermore, the camera is cooled to -5 deg celsius to reduce the amount of noise generated while imaging.

The steps followed for imaging each of the TEM grid are (i) refill of liquid nitrogen for the microscope, (ii) loading (or reloading) the specimen on the holder and system pump-down, (iii) setting aperture and aligning the objective lens, (iv) monitoring FFT of live images for stigmation errors, and (v) adjusting the image focus. Steps (iv) and (v) are repeated at the target locations on the sample holder, as described in section 2.8. The batch converted files are then used for post processing, as described in sections 2.8.1 and 2.8.2.

One drawback with using TEM for studying the flame generated soot is that this method has been shown to deface the structure of the primary particles [24]. This is predominantly due to the intensity of the powerful electron beam, and the amount of time that the sample is exposed to this beam. Therefore, the TEM grids are exposed to (1) the least electron beam intensity that can provide adequate contrast for imaging, and a uniform background; and (2) shortest imaging time possible to generate adequate images to generate sufficient images to obtain sufficient number of samples for providing the required particle size distribution.

2.7.2 Broadband Flame Luminosity Measurements

Line-of-sight integrated flame luminosity measurements is acquired with the help of high-speed sCMOS camera (Andor Neo 5.5) through an objective lens (85 mm, f/# = 1.8). The image acquisition at 100 fps yields a 2K resolution images with an exposure time of 1ms, which provided good dynamic range without saturating the sensor. A sequence of 475 images were captured at each condition. Additionally, broadband images of soot were used to help optimally deploy the TSS system in the LFB. While the raw LII decay signals used

to determine the targeted least sampling HAB, high-speed broadband images were acquired to determine the sampling duration and the images of TSS operating in the LFB.

2.8 Data Analysis

The samples collected on the TEM grids is processed viewing them in a TEM. A set of 50 - 75 images is acquired at varying magnification, depending on the morphology, for each of the tested conditions. Five regions, as shown in Figure 2.14, are chosen on each of the TEM grids to obtain the images. This is achieved with the help of TEM user interface software, that controls the position of TEM grid holder. Quantification of the acquired data involves obtaining the statistical average size of soot particles to see its variation with HAB, equivalence ratio and pressure. To achieve this, the size distribution is obtained by post-processing the acquired data with the help of imageJ software, as described in subsection 2.8.1. The size distribution is created by manually selecting the 500 - 550 samples of fully matured, unambiguous particles from the TEM images each test condition.

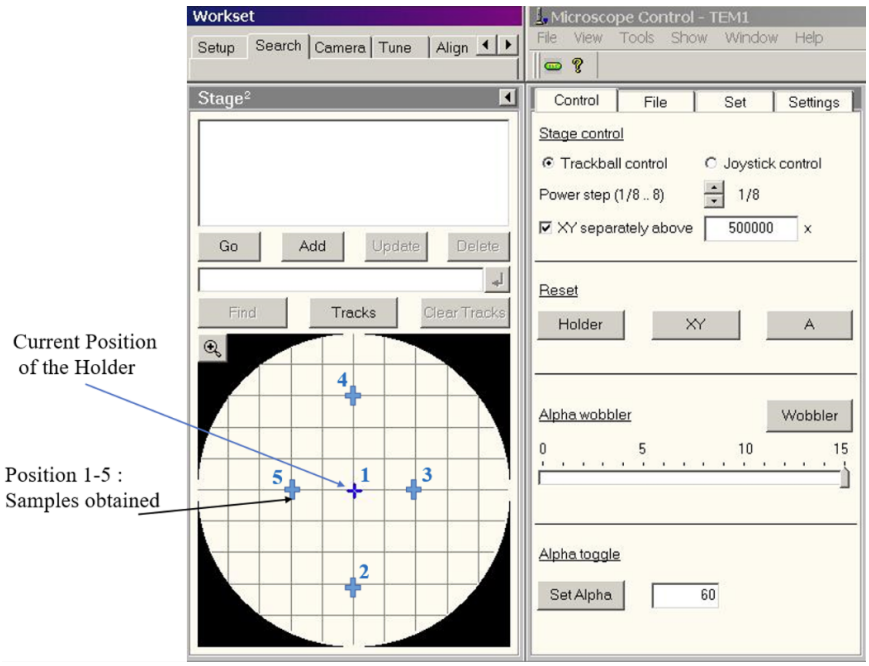

Figure 2.14: Regions of data acquisition on the TEM grid.

2.8.1 Post-processing

The obtained batch-converted raw images are post processed with the help of imageJ software. The steps involved in this process are represented in Figure 2.15. Initially, the dimension for a each pixel is determined from the provided length scale, as shown in Figure 2.15a. Unambiguous soot particles are then identified, and their size is measured. This is depicted in Figure 2.15b. These measurements generate the raw data, that are statistically processed as described in subsection 2.8.2, to study the variation particle size.

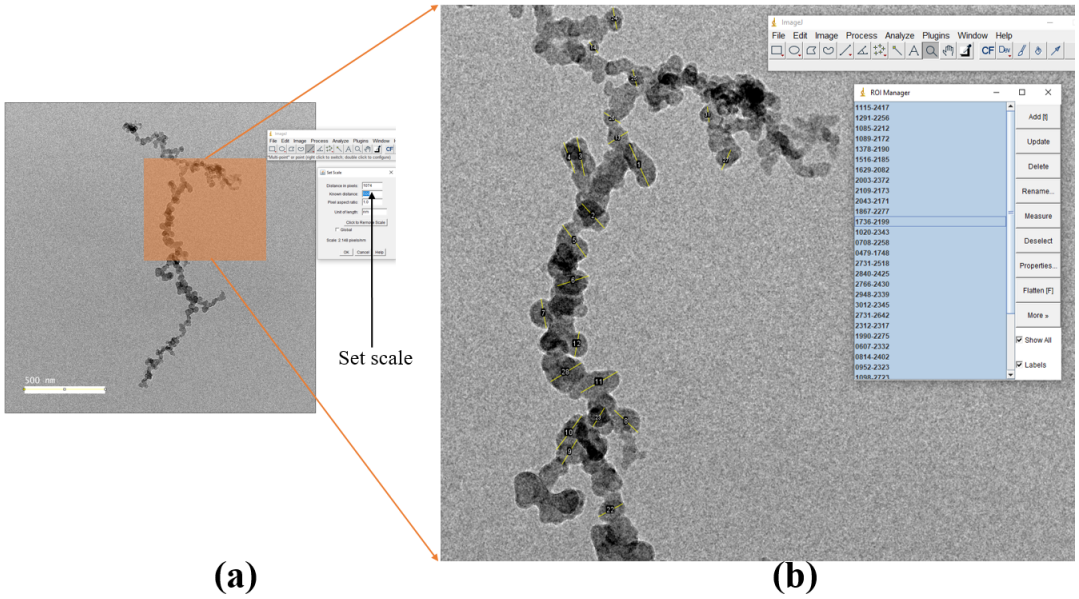

Figure 2.15: ImageJ software post processing: (a) set scale; (b) identify particles and measure

2.8.2 Statistical Processing

Upon generating the raw CSV file from imageJ, the data is processed in Matlab software to determine its statistics. From the generated histogram, the relative frequency of occurrence and the probability density function is calculated. The first and second order moments are computed from this distribution to obtain the mean particle size, and its standard deviation. Finally, a select set of conditions were repeated to see if the obtained data qualitatively resembles the particle size distribution obtained during the first iteration.

2.9 Limitations of the Setup

The limitations of the LFB and the TSS system are described in this section. As stated before, the LFB was designed to target an equivalence ratio of 1.5 at 8 bar pressure. The estimates were based on the computational simulations for flame speed data that were obtained from Chemkin software. While testing, it was found that the flow metering equipment were not sufficient to provide sooty flames at elevated pressures above 40 psig. A rotometer capable of providing higher flow rates of fuel is required to achieve this. However, reproducible results for sooty flames were obtained until 40 psig pressure, which is the current upper limit of operation for the LFB. Furthermore, the PID controller that is used to control the preheat temperatures of the unburnt mixture produced a temperature variation of 10 K. This was observed to have noticeable effect on flame structure, and thereby soot production.

Although this type of soot sampling provides the capability for in-situ analysis, the limitations associated with the imaging technique allows only for a 2D projection of the 3D particles, is a major limitation. As a result, about 30 % of the soot chains were ignored because the obtained images were unclear due to its complex morphology in the third dimension, which caused the particles in the chain to be unclear.

One of the major operational limitations of the soot sampler system setup is its inability to collect samples at atmospheric pressure at the sampled HAB in this study. The required sampling time is large enough to damage the TEM grids. The TSS system is designed to be modular, however, replacing the TEM grids through the windows was not achieved. This meant a long over haul time for replacing the TEM grids. Exposure of the SA to the secondary reaction zone caused damage to its components, so reducing the number of sampling arms is preferred. Finally, while the operation of the soot sampler is confirmed at high pressure, the temperature constraint of the motor is a major limitation considering its operation in the vicinity to the flame.

CHAPTER 3

RESULTS AND DISCUSSION

Qualitative results of the investigation presented in sections 3.1 and 3.2 include (i) structure of the flame exhibiting instabilities; (ii) types of particles present in the extracted samples; and (iii) the dominant morphological characteristics of the flame-generated soot particles. The complicating effects on LII signal interpretation are also discussed. Furthermore, the effect of pressure, equivalence ratio, and the sampling HAB on soot production are quantified by analysis of mean particle size in section 3.3.

3.1 Flame Structure

The camera line-of sight integrated flame luminosity data (Figures 3.1 and 3.2) have the same intensity scale to qualitatively compare the manifestation of the instabilities. Figure 3.1 shows changes in the flame structure for increasing equivalence ratio. This image

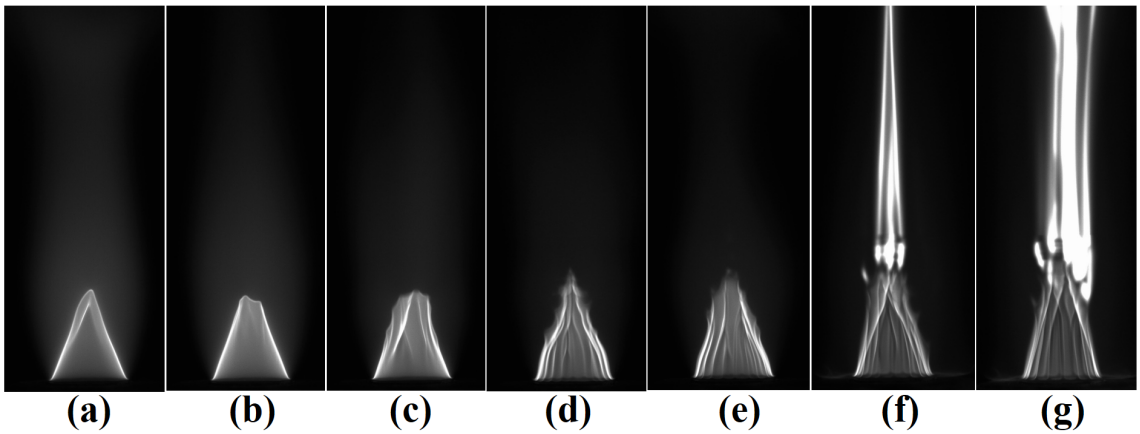

Figure 3.1: Growth of cellular instabilities with increase in equivalence ratio (at 20 psig, and a preheat temperature of 205 K): (a) ϕ=1.30; (b) ϕ=1.36; (c) ϕ=1.41; (d) ϕ=1.46; (e) ϕ=1.51; (f) ϕ=1.61; (g) ϕ=1.81.

set depicts the transition from a smooth conical flame into a wrinkled flame. This is because of the onset of thermal-diffusive instabilities. The deflagrations of rich jet-A/air premix-

tures is limited by the lighter species, thus causing these instabilities to manifest. For the flame under investigation, these non-uniformities exist in the form of straight ridges around the circumference, with a width of 3-4 mm. These flame characteristics are consistent with previous findings [16, 19, 69].

Law et al. [69] observed similar behavior for rich premixed propane-air flame, and established that these structures existed at low premixed gas velocity at the burner nozzle exit. Finally, the presence of secondary reaction zone as observed in Figure 3.1a-e, is attributed to the combustion of unburnt fuel in the products of the fuel rich premixed flame. As seen in Figure 3.1f-g and Figure 3.2, this zone is not visible as soon as the soot production started.

The phenomenon responsible for flame-tip breakup [69], as observed in higher equivalence ratios (from Figure 3.1c-g), is the same as that of tip-opening of a Bunsen flame. For a mixture comprising of deficient species that have higher mobility, local flame extinction at the tip is the is the result of differential diffusion. The corrugated nature of the flame, combined with the tip extinction, results in the formation of sooty streaks, as shown in Figure 3.1-f,g, and Figure 3.2.

Occasionally, the instabilities cause these circumferential ridges to rotate about it vertical axis (see Supplementary material - ϕ2.19.gif). For varying conditions, the direction and rate of the rotation of these structures are not constant. Furthermore, the HAB at which soot production started, is found to exhibit unsteady behavior which is also observed in ϕ2.19.gif. This is attributed to the coupled effect of vibrating flame instabilities [20], which is the direct effect of unsteady heat loss.

For further increase in ϕ, the instabilities in the flame begin to diminish. This is represented in Figure 3.2. The structure of the flame transitions from corrugated ridges to that of a smooth bulk flame. Additionally, the flame is also observed to form cusps. These are responsible for the spitting nature of the soot, which is observed as the high density transverse troughs in the sooty streaks, as seen in Figure 2.10. The frequency of this spitting behavior decreased with increasing equivalence ratio. Finally, for varying ϕ between 1.6

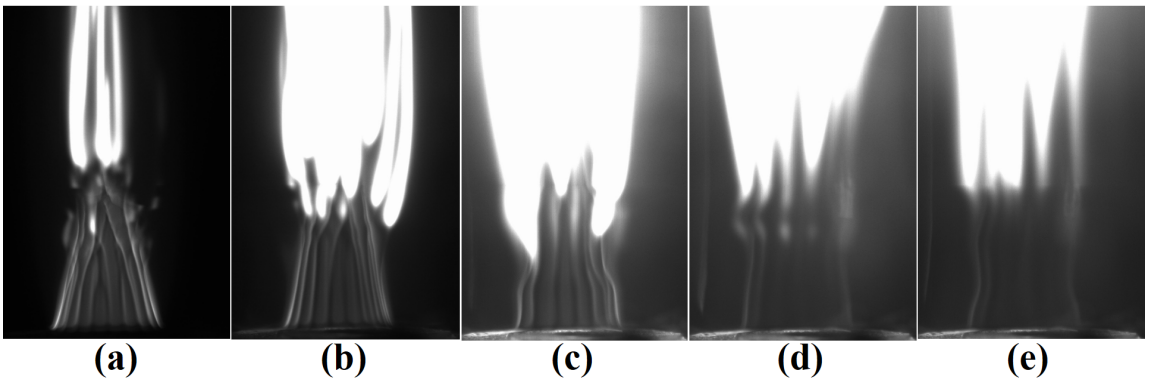

Figure 3.2: Decrease of instabilities with further increase in equivalence ratio (at 20 psig and a preheat temperature of 200K): (a) ϕ=2.1; (b) ϕ=2.29; (c) ϕ=2.48; (d) ϕ=2.64; (e) ϕ=2.81.

and 3.2, the residence time for soot formation (height at which soot production starts) is observed to be constant. Considering the nature spatio-temporal nature of the flame, the produced soot particles can exposed to a PAH filled environment, which are identified to be one of the causes for soot particles to restructure.

The description above pertains to flames at elevated pressures. The soot production at atmospheric pressure exhibited most of the above-mentioned behavior, with difference in the threshold of ridge formation. While the laminar flame at elevated pressures have multiple ridges at soot inception, the flame at atmospheric pressure was observed to have two diametrically located streaks, as seen in the flame structure of Figure 2.13. Moreover, the number of streaks were found to increase with increase in equivalence ratio.

This flame behavior complicates the implementation of the diagnostics. For the extractive soot sampler, the sampling duration of 125 ms is found to be sufficiently long to collect data from the flame. This is determined through trial and error, as longest delay time that can extract soot samples with intact TEM grids. Furthermore, this flame characteristic also requires a large ensemble of LII signals to appropriately calibrate the acquired optical measurements.

3.2 Characteristics of Flame Generated Particulate Emission

The physically extracted particulate matter are analyzed through TEM imaging. This section details various qualitative aspects of the obtained data along with their classification. Existence of soot particles and non-soot organic matter are identified, and their morphological characteristics are also detailed. Finally, findings from literature that include (i) HRTEM and Raman spectroscopy [70]; and (ii) TEM-EDX (transmission electron microscopy- energy dispersive x-ray) spectroscopy [71] are leveraged to hypothesize the elemental composition of the particles through their structural resemblance.

3.2.1 Soot Particles

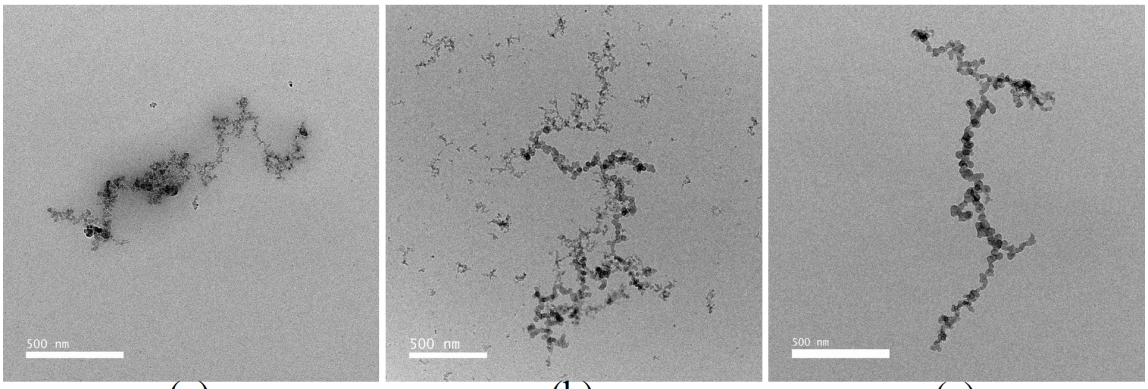

Figure 3.3: Primary soot particles of varying sizes.

The elemental composition of primary soot particles, shown in Figure 3.3, are C as its major composition, with minor presence of O, and H [72]. The primary particles are observed to have size varying between 10 - 75 nm. An important characteristic of the soot particles is that they form chains or aggregates with one another.

Recent studies by Hu et al. [70] investigated the effect of pressure and inlet temperature on soot production in a jet stirred reactor burning aviation kerosene. The nanostructure of these soot particles was investigated by HRTEM and Raman spectroscopy.

The HRTEM results indicated that the primary soot particles exhibited shell-core nanostrucures, with graphitized outer-shell and multiple inner cores that were reactive in nature. The Raman spectroscopy, on the other hand, revealed the absence of amorphous carbon at elevated pressures. The combined effect of these findings can explain the formation of glob-like structures at elevated pressures, as shown in Figure 3.4; through the collapse of such chemically-reactive inner-cores [70]. Furthermore, based on their structural similarity to TEM-EDX studies in the literature [71], these particles are hypothesized to have O and C as their dominant elemental composition, as opposed to primary soot particles that are excessively dominated by C.

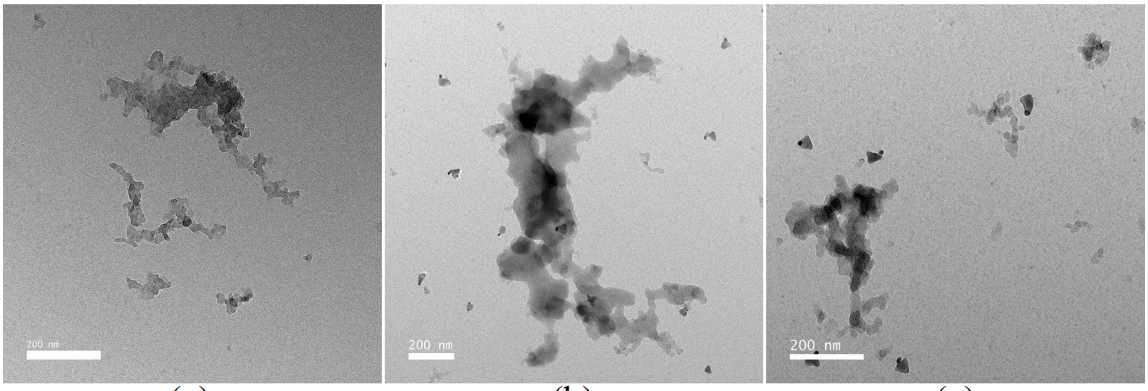

Figure 3.4: Presence of soot globs:(a) at 20 psig; (b),(c) at 40 psig.

Cumulatively, all the soot particles are observed to have of size varying between 10 - 250 nm. Although the range of the sizes is in agreement with studies from the literature for liquid fuels that contain aromatic hydrocarbons (for example diesel, gasoline, etc.) [38, 53], the internal structure of the primary soot particles, that is responsible for its reactive nature, is unique in jet-A combustion [70].

3.2.2 Non-Soot Particles

Apart from the presence of soot particles that readily form aggregates, presence of other non-soot particulate matter are noted along with their possible composition. These include

(i) fibre-like structures; (ii) spherical non-soot particles of uniform contrast; (iii) spherical non-soot particles of non-uniform contrast; and (iv) sharp contrasted mineral-like particles. The presence of these types of particles have been noted in the emissions of (i) diesel and natural gas powered engine [38]; (ii) gasoline (and diesel) powered combustion [73], and (iii) coal powered combustion plants [71, 74].

Fibres

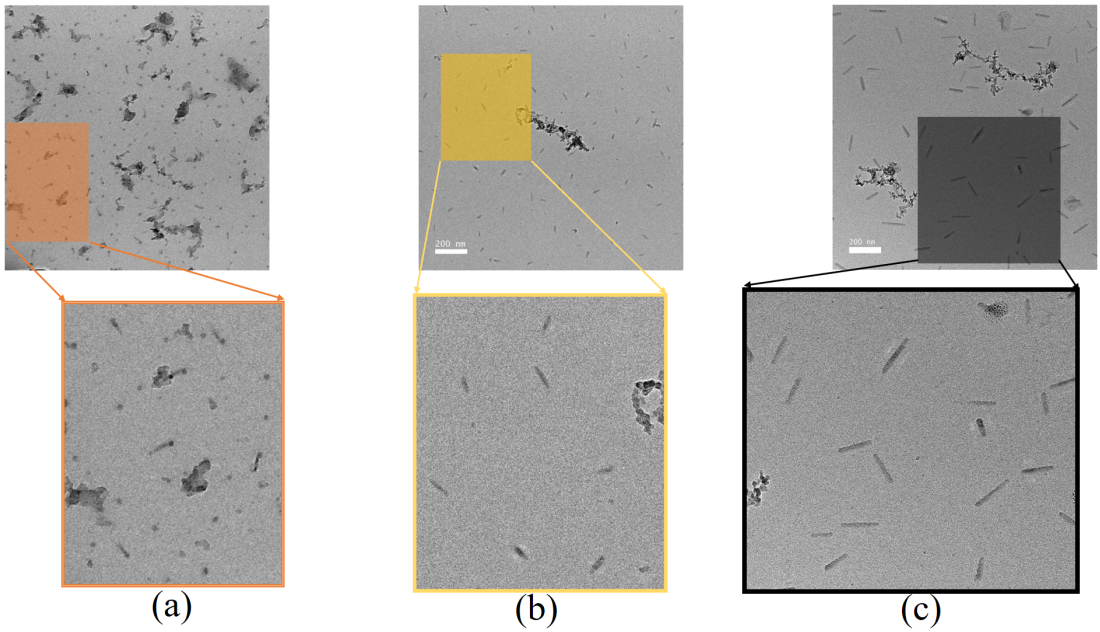

Figure 3.5: Fibre-like particles of varying lengths and maturity.

Figure 3.5 shows the presence of fibre-like structures of varying length for different test conditions. These particles are present in 17% of the conditions tested. In most of the test cases, these fibres are separated by soot aggregates, which is consistent with the findings of particulate emissions from natural gas fueled marine engines by Baldelli et. al. [38]. The presence of Fe bearing nanoparticles have been reported in both diesel and gasoline vehicles [73]. The fibre like particles are most likely carbon-nanotubes [75, 76] or geoethites [73], that could be produced because of the presence of Fe [38]. Furthermore, the possibility of Fe is claimed based on the presence of homogeneous, almost spherical particulate matter

as shown below.

Spheres

Several instances of spherical particles have been noted in the literature [38, 71, 73, 74, 77]. Multiple occurrences for two types of spheres is observed in the collected samples: (1) uniform, almost spherical particles that have diameter <65 nm , as seen in Figure 3.6; and (2) non-homogeneous spherical particles of varying contrast, as shown in Figure 3.7, that typically have diameter ∼200 nm.

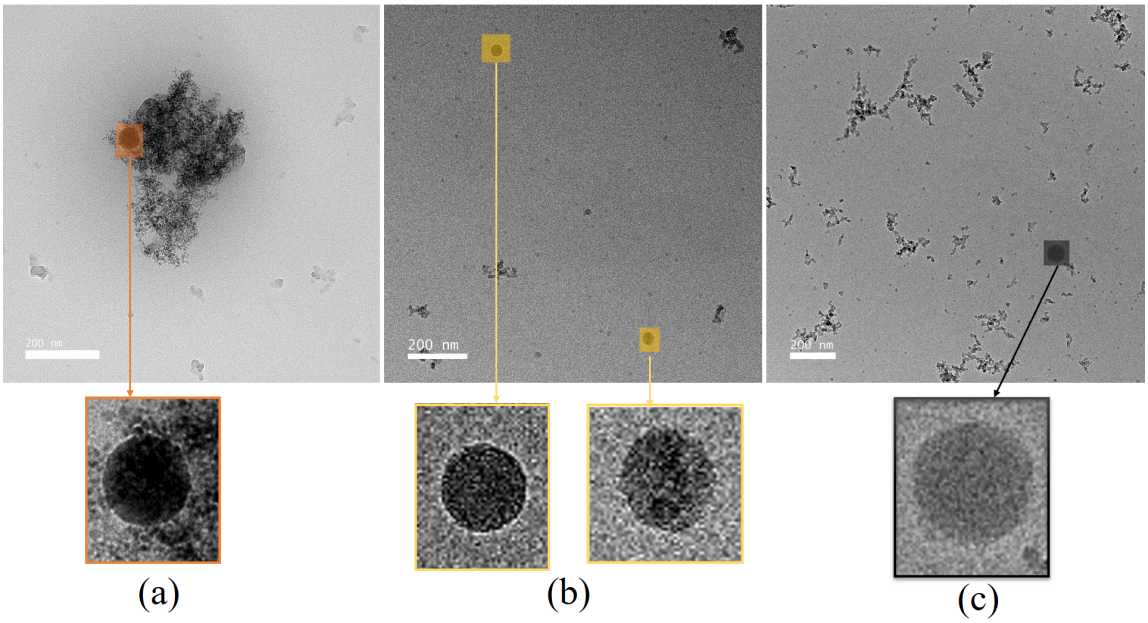

Figure 3.6: Presence of uniform spherical non-soot particles in: (a) cluster formed by small primary soot particles; (b),(c) - as solitary structures.

Xing et al. [42] observed particles that are of the same sizes as those observed in this investigation, whereas Baldelli et. al. [38] observed similar spherical particles with larger diameters of ∼190-350 nm. The dominant elemental composition of the uniform spherical particles is either (i) Ca with some P and O [38, 42, 78]; or (ii) Fe [42, 71, 74].

Multiple occurrences of porous spherical particles with varying contrast is shown in Figure 3.7 and Figure 3.8c. Several studies in the literature attribute these structures in an organic matter to the elemental composition dominated by S [71, 74, 78]. However, Dahl

et. al, [77] produced structures exactly like the data observed here, but the composition of these structures were inconclusive.

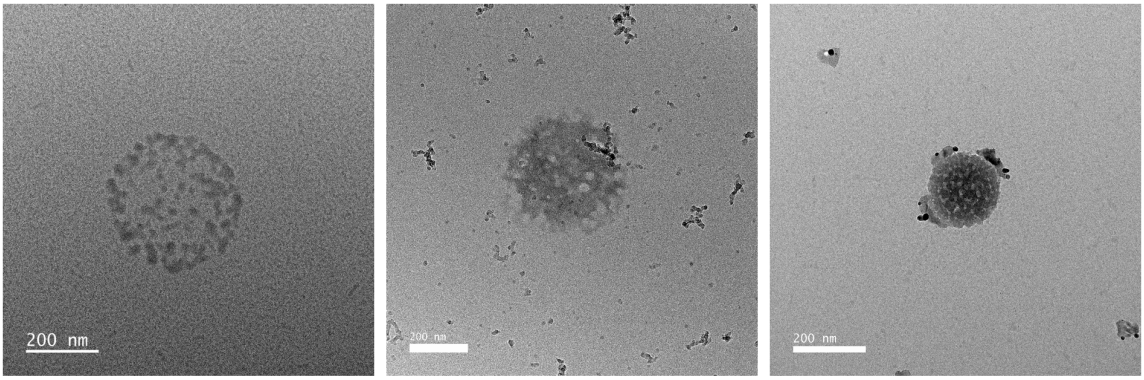

(a) (b) (c)

Figure 3.7: Porous spherical particles with varying contrast as observed in the data.

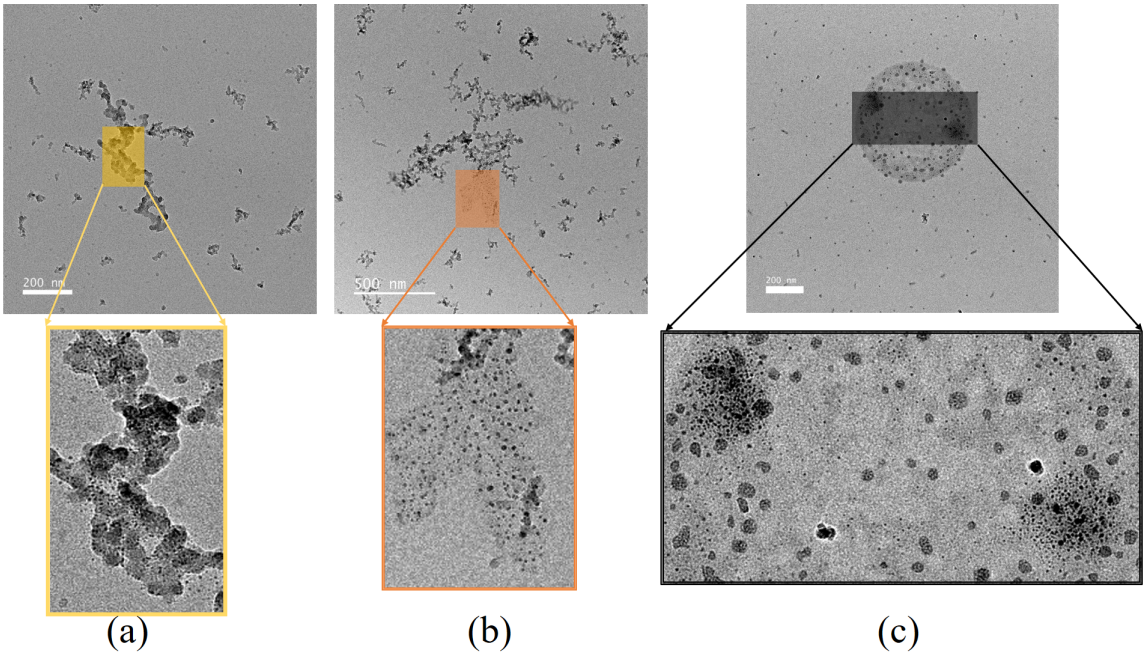

(a) (b) (c)

Figure 3.8: Sharp contrasted mineral-like particles.

Minerals

Some of the samples contained clusters of small particles less than 3 nm in diameter are observed. These particles have a strong contrast that due to strong electron scattering, that is typical of metals or minerals. Furthermore, the presence of mineral like particle clusters

is observed to occur in two scenarios: (1) mixed with soot or other organic matter, as shown in (Figure 3.8a, c); or (2) surrounded by darker grey area (Figure 3.8b), which is indicative of volatile organics [38, 79]. In this case, although the particles do not have any indication of volatile organics, still exist in clusters with close proximity to each other as depicted in the figure.

The presence of soot, as well as various non-soot particles is noted in Sections 3.2.1 and 3.2.2. The substantial presence of non-soot particles play a role in interpreting the LII signals through (i) contaminating the incandescence decay, and (ii) absorbing a considerable part of the incident prompt laser signal. The soot particles, on the other hand, are observed to have varying contrast because of the considerable difference in their size and composition. These will affect the temporal decay of their incandescence signal due to the difference in its signal absorption and heat transfer. Furthermore, their morphological characteristics, described in subsection 3.2.3, are also expected to contribute to the complexity associated with the interpretation.

3.2.3 Morphological Characteristics of Soot Particles

The morphological characteristics of the soot refer to the type of chains and aggregates formed by its constituent particles. Some of the traits, like those observed in Figures 3.9, 3.12 and 3.13, are similar to that of diesel particulate emissions found in the literature [70, 80–82]. One of the dominant aspects of soot chains is its complex morphology, which is attributed to the coupled effect of aggregate formations between primary particles and glob-like soot particles (Figure 3.9a), and restructuring (Figure 3.9b). While the presence of glob-like like structures in the chain are because of their aggregate formation with chains of primary soot particles, the effect of restructuring is attributed to the exposure of soot clusters to the combustion products like water-vapor, sulfuric acid, etc.

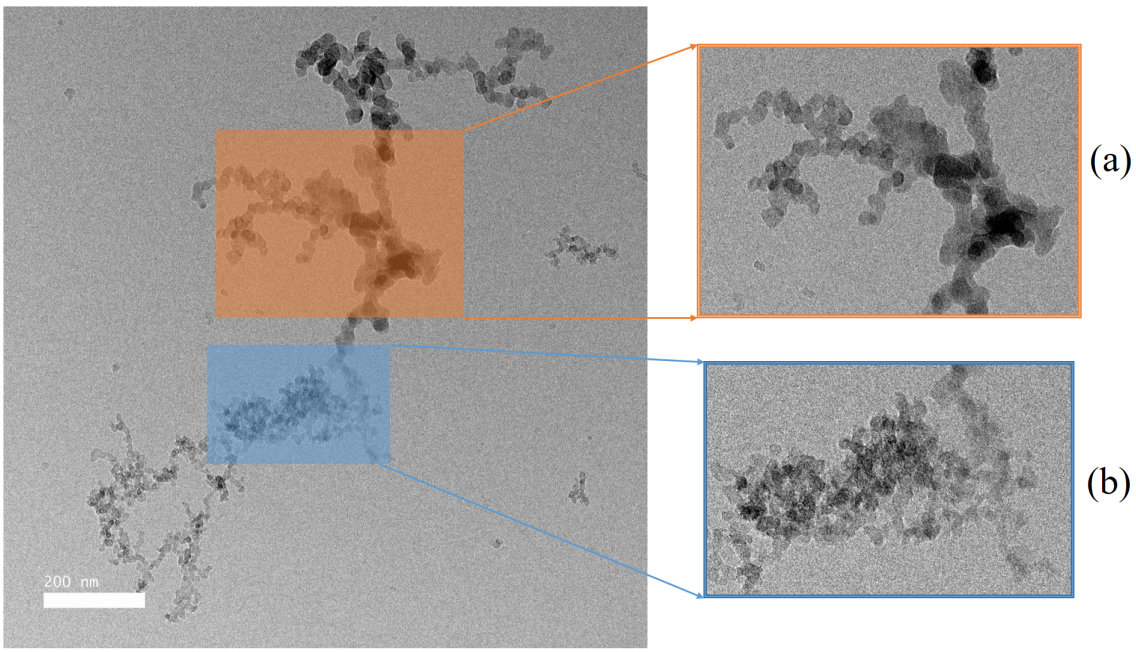

Figure 3.9: Presence of complicated long chains of soot particles: (a) Glob-like particles as a part of chain; (b) Restructured soot aggregates.

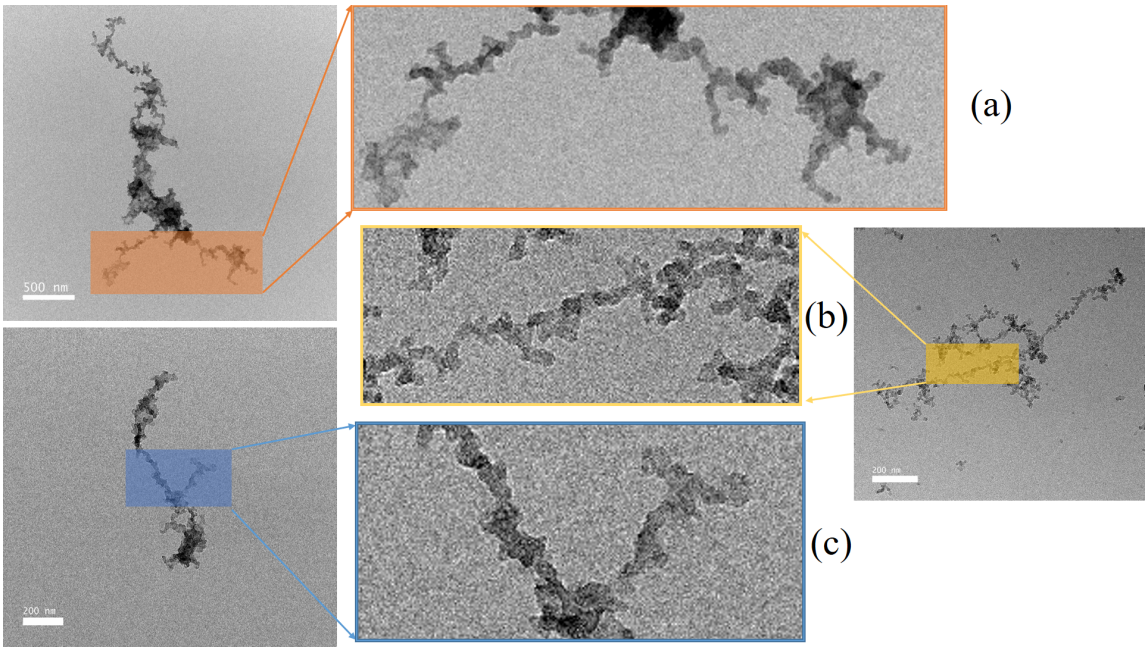

Figure 3.10: Coalescence of primary soot particles leading to ligament like structures of long soot chains.

The other dominant aspect that is associated with restructuring, and also chemically reactive soot particles is the coalescence of multiple soot particles to form ligament like

structures as shown in Figure 3.10. While the glob-like soot formation is attributed to the reactive soot particles in an aggregate cluster, the reactive nature of the soot particles in the chain can explain the formation of these ligament like structures.

Apart from forming complex chains, several instances of long chains of primary soot particles are also observed (see Figure 3.11, Figure 3.3). The typical chain lengths for these structures are in the order 1.5 μm. Long chains of soot particles with varying sizes causes the chains to form bent structures, as shown in Figure 3.11. Furthermore, they are also observed to form several branches which also tend to exhibit similar characteristics. These branched chains eventually attach to other soot particles in the parent chain to form closed structures as shown in Figure 3.12. This morphological behavior is consistent with the observations made on diesel/n-octonol mixtures be Zhou et al., [83]. The exposure of these closed chains formed by soot particles tend to restructure and further complicate its morphology.

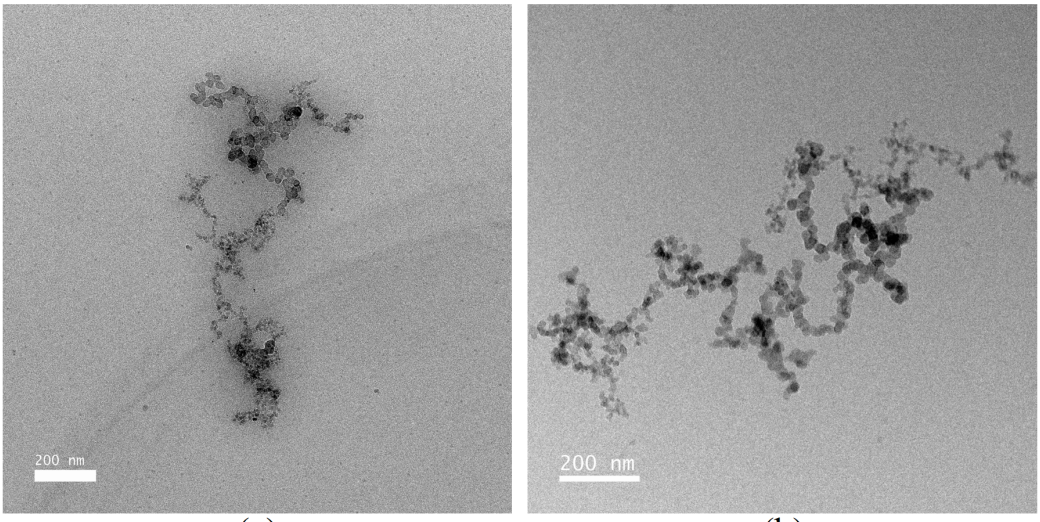

(a) (b)

Figure 3.11: Simple long chains formed by primary soot particles, and branched soot chains - having bent structures.

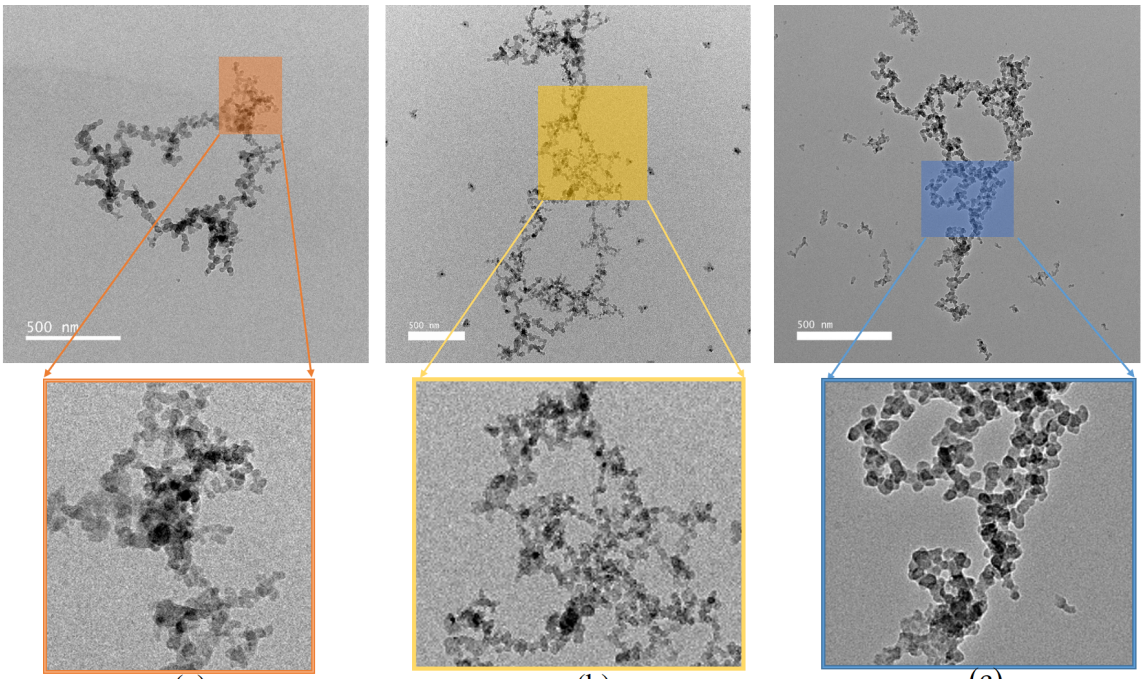

Figure 3.12: Attachment of branched soot chains to the parent chain to form closed chain : behavior exhibited by (a) glob-like soot particles; (b) & (c) primary soot particles forming restructured particles.

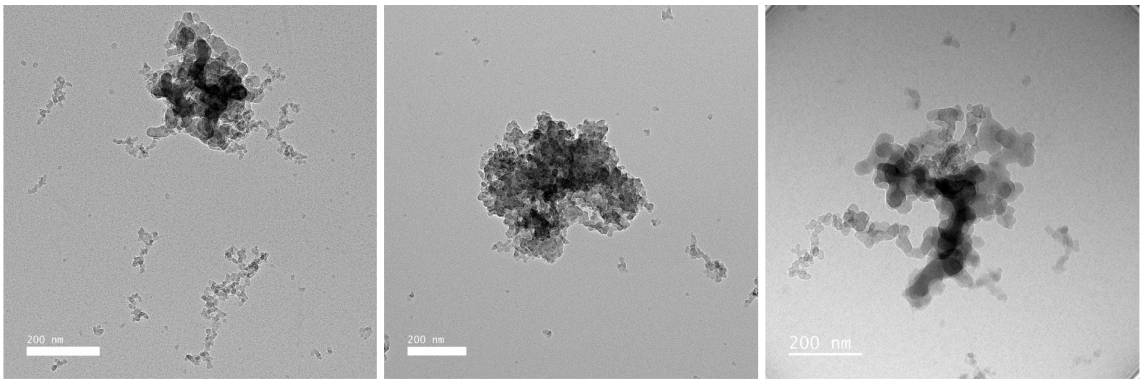

Figure 3.13: Presence of compact aggregates as described by [38]

Finally, the presence of compact aggregates less or no internal voids, as seen in Figure 3.6a and Figure 3.13 respectively, are found in several instances. Baldelli et al. [38] observed similar structures, and referred to these as *small-compact aggregates*. The compaction of these aggregates was hypothesized to occur upon (1) evaporation or condensation

of volatile material [84]; (2) highly-oxygenated hydrocarbons [38, 85]; or (3) restructuring due to sulphuric acid [38, 86].

While the complication associated with interpreting the LII signal because of individual nvPM was noted at the end of subsection 3.2.1, it is important to account for the effect of the morphological characteristics as well. Apart from the shielding effect from aggregates of primary soot particles, the restructuring effect of soot particles add additional complexities to interpreting the obtained LII signals through non-uniformity in the optical properties of soot change due to (1) restructuring of soot chains that form clusters of varying density, and enhanced shielding effect; and (2) compact structures that resemble like one glob-like particle.

3.3 Quantitative Results

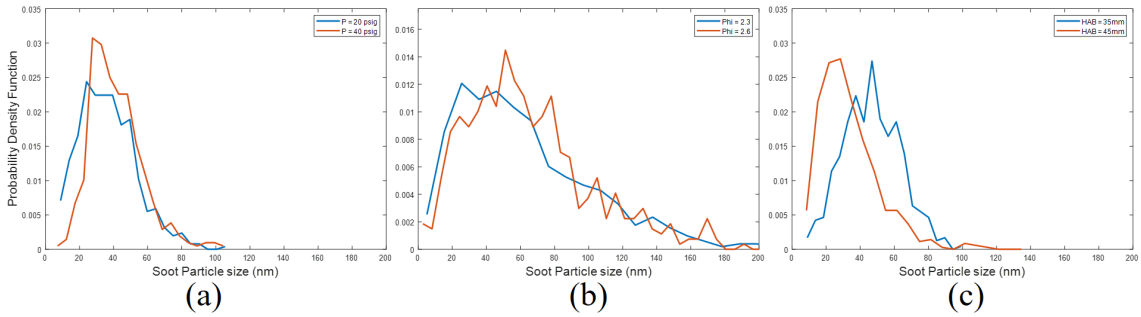

Figure 3.14: Probability density function for varying (a) pressure; (b) equivalence ratio; and (c) height above the burner.

The quantitative data presented for this study includes (i) Probability Density Function (PDF) of the particle size distribution, which is used to compute the mean particle size; and the (ii) variation of mean particle size with pressure, equivalence ratio and height above the burner. Figure 3.14a-c shows the variation of the PDF with these parameters. Figure 3.14a shows the distribution at varying pressures for an equivalence ratio of 1.6 and 35 mm HAB. The distribution is observed to have a relatively higher mean particle size at higher pressure, that is consistent with the findings of Hu et. al. [70]. It should also be noted that the most

probable size from the size distribution is in between 20 - 30 nm. Figure 3.14b shows the distribution for varying equivalence ratios at 40 mm HAB, and a pressure of 20 psig. While the most probable size at ϕ = 2.3 is between 20 and 30 nm, the distribution at ϕ = 2.6 is shows a most probable size between 50 - 60 nm. A similar trend is observed for varying HAB at an equivalence ratio of 2.9, and 20 psig pressure.

The PDF of these distributions were found to be unimodal with kurtosis close to 3. Therefore, the particle size is assumed to be a normal random variable. Hence, the gaussian assumption is used to provide the standard error in the mean value of the size distribution, seen in Figure 3.15 and Figure 3.16. The plots presented here follow a key: the circular data points (o) represent the data obtained at a pressure of 40 psig, and the asterix (*) represent the data points at 20 psig. The sampling height is color coded as HAB = 45 mm, in red; HAB = 40 mm, in blue; and HAB = 35 mm, in black.

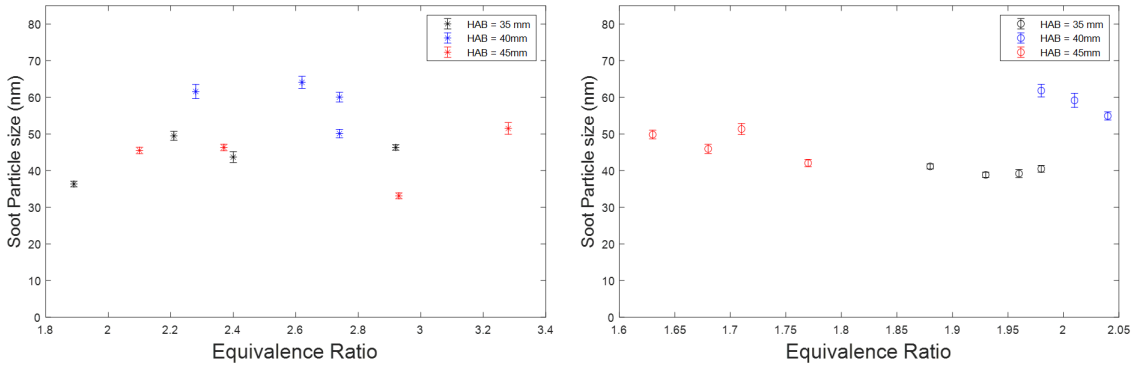

Figure 3.15: Variation of mean soot particle size with equivalence ratio at elevated pressures: (a) 20 psig; (b) 40 psig.

These data show an initial increase in soot particle size with height, which is attributed to the particle size growth through agglomeration. Subsequently, oxidation of the soot particles causes their size reduction with height. Although this could explain the behavior, considering the 10 mm range of sampling HAB as compared to a much longer flame, there is a possibility that this trend is indicative of inconclusive variation. Moreover, the data presented for varying equivalence ratio do not show a global trend either. These can attributed

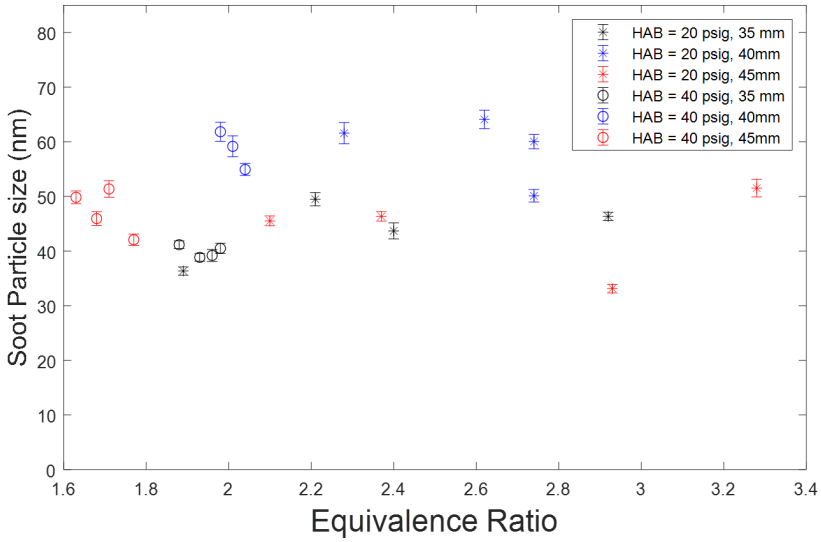

Figure 3.16: Global variation of mean particle size

to the effect of varying preheat temperatures and soot restructuring due to a significantly long exposure time.

Two data points that were acquired at a same equivalence ratio (ϕ = 2.74) at 40 mm HAB for the flame at 20 psig pressure. The difference between these conditions is their preheat temperatures of 217K and 210K, which yielded mean particle sizes of 60.05 nm, and 50.11 nm, respectively. Hu et al. [70] attributed the reduction in particle sizes at lower preheat temperatures to reduced graphitization at lower temperatures. Figure 3.16 shows that the particle size at 40 psig, in general, yielded higher magnitudes for mean particle size than that of 20 psig. Therefore, it can be concluded that the soot particle sizes increase with increase in pressure. This is consistent with the findings of Hu et. al [70], which can be attributed to the particles having more mature nanostructures.

CHAPTER 4
CONCLUDING REMARKS

This research documents the findings from the study of soot production in premixed jet-A/air laminar flames at elevated pressures, which hasn't been examined before. The objective of this investigation was to design and deploy a thermophoretic soot sampling system that extracts soot samples in a premixed flame which burns liquid jet-A fuel at elevated pressures, to study the effect of pressure, HAB, and equivalence ratio on the particle size. The data provided in this study will also be used to interpret and calibrate the simultaneously obtained TiRe LII signals. The combustion process studied here are relevant to potential future combustors burning fuel-lean premixed flames for supersonic transport engines. Although the combustors are theoretically lean, soot production for a premixed flames requires fuel-rich premixtures. So, rich mixtures of prevaporized jet-A and air were used to obtain an axisymmetric, laminar sooty flame, on which the TiRe LII signals are calibrated.

An existing burner was refurbished, and redesigned to achieve this objective. Accurate flow metering allowed for obtaining unburnt, heat traced fuel-oxidizer premixtures for ϕ varying between 1.6 and 3.3 that produced rich, sooty flames upto 40 psig pressure. Because of the low velocities of the unburnt gases, the flame was found to exhibit thermal-diffusive instabilites that caused it to have reproducible corrugated structures that exhibited spatial and temporal variations. The above-mentioned in-situ diagnostics was performed on this flame.

The thermophoretic soot sampling system with a rotating sampling disk, similar to [56] was custom designed and deployed in the burner. 5 of the 10 sampling arms were used to obtain data for each of the test conditions to study the dependence of mean soot particle size on (i) sampling height above the burner - 35 mm, 40 mm and 45 mm HAB, (ii) ϕ

varying between 1.6 and 3.2, in a (iii) pressurized environment of 20 psig and 40 psig that lead to a total of 24 test conditions. It was found that the sampling time for the soot sampler was significantly larger than the data found in the literature, which would affect the nanostructures of soot particles due to enhanced restructuring. The collected samples were then analyzed, and found to exhibit an increasing-decreasing variation with height which can be attributed to agglomeration, and oxidation of soot particles at the least, and highest HAB respectively. However, considering the small range for sampling HAB, coupled with the restructuring nature of the soot, an inconclusive behavior for soot particle with HAB is a possibility. The size of the soot particles exhibited direct correlation with the ambient pressure. Enhanced extent of graphitization, and increased maturity in the nanostructures of the soot particles are identified to be the reasons for this behavior. Finally, the preheat temperature was also observed to have an effect on particle size.

Morphology of the soot particles that include coalescence of primary particles to form ligament like structures, closed chains, and presence of compact aggregates similar to [38] were identified. These were explained as the coupled effect of chemically reactive nature of the soot particles, and restructuring because of the exposure of these soot particles to PAH, water vapor and sulphuric acid. Presence of non-soot particulate matter and their hypothesized constituents were presented. These include: (1) spherical particles of uniform contrast - Fe (or) Ca with P and O; (2) porous spherical structures, identified as sulphur; (3) fibre-like structures - attributed to wither CNT or geoethite; and (4) mineral like structures - that occur as clusters in soot, volatile organics or non-soot particles. Although there are similarities between particulate emissions and morphology of soot produced by jet-A and (1) coal and diesel the nano-structures of the soot particles are understood to be different, and responsible for properties observed in this study.

Finally, in addition to accounting for the shielding effect because of the aggregate forming nature of flame generated soot, the presence of various organic matter and non-soot emissions can exacerbate the difficulties associated with interpreting the TiRe LII signals.

The chemically reactive soot particles and their morphology can cause drastic change in the optical properties due to (1) non-homogeneous particles that cause non-uniform absorption and emission of radiation; and (2) complicated heat transfer as a result of complicated morphological characteristics. It is believed that the data provided in this investigation will help with (i) calibration and interpretation for the optical measurements; and (ii) validation for computational studies.

4.1 Recommendations for future scope

By ensuring adequate mixing of prevaporized mixtures the onset of soot production in combustion process can be delayed. Although there are several studies in the literature that investigate the process of soot production, it is still not very clearly understood. The present research along with recent findings [70] reveals the presence of chemically reactive soot particles for jet A, affecting the particle size and its morphological characteristics. Furthermore, presence of wide range for the size for primary soot particles invalidates the monomer-based models for estimating the morphological characteristics. This mandates the need for advanced models for soot particle formation and oxidation for complex fuels, and their morphology.

Although this technique extracts in-situ samples, the drawback associated with planar projection on TEM to obtain the characteristics is not sufficient to provide all the details. This can be overcome by leveraging the 3D scanning transmission electron microscopes (STEM). Furthermore, the presence of non-soot particles and its potential elemental composition is proposed in this study. Moving forward, it is important to use appropriate techniques that can give the composition of particles while dealing with complex fuels that contain aromatic species that readily form PAH. Recommendations for the techniques include (i) HRTEM to better understand the nanostructures of the particles, (ii) TEM with EDX (energy dispersed x-ray) studies, (iii)X-ray spectroscopy studies etc.

The major limitation was the operational range of the current experimental setup. The

possibility of using a rotometer that can deliver higher flow rate of fuel should be explored. Additionally, increasing the preheat temperature is also be recommended. The study on jet stirred reactor showed low maturity for the soot particles at low inlet temperatures. The issue faced during the experimentation was that at higher preheat temperatures, the flame flashed back frequently due to the increased the flame speed. This can be overcome with higher gas velocities, which further increases the HAB at which soot is produced; thus also mandating the need for thicker spacers shown in Figure 2.1.

Appendices

APPENDIX A

INSTALLATION OF THE TSS SYSTEM

The components of the TSS system are designed based on the preliminary assembly estimates obtained from the Autodesk Inventor assembly files. The diameter of the sampling disc base plate, along with the width and length of the arms were sized in such a way that the TEM grids (and the base plate) are not exposed to the pilot flame during its resting phase. The design of other components (like shaft-extension, anchor, etc.), and their mounting axis were determined by the projection of the burner nozzle exit and its proximity to the cross-sectional plane of the leading face. Figure A.1 is the schematic of the installation of the TSS system components along with its mounting sequence to the LFB. With exception of the gearbox anchor, all the components are modularly designed to be dismantled into individual components that facilitate quicker overhaul for change of TEM grids, or modifications as required.

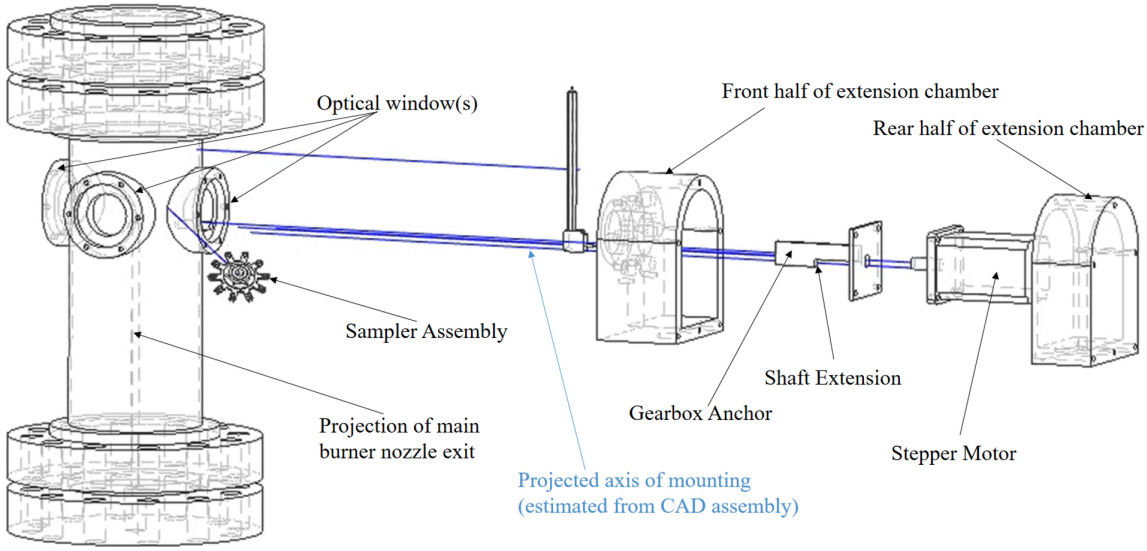

Figure A.1: TSS system - LFB assembly projection.

The installation of the TSS consisted of several steps. At first, (i) the front half of the

extension chamber is installed with a 1/16 inch thick grafoil sheet in on the outermost face of the optical window (the face that contains the bolt pattern). This part of the chamber is secured in position with 6 high-shear 1/4-20 bolts. The stepper motor-drive train assembly, shown in Figure 2.5 (without the sampler assembly and hexagonal shaft), is then installed by securing it in the designated threaded holes in the interior face of the this half of the extension chamber. This assembly is the heart of the TSS system, consisting of the motor shaft extension, gearbox and the hexagonal shaft (installed at the end, just before the SA).

The design of motor-shaft extension is similar to that of a shoulder bolt, except for its head. The end face of the shaft from the stepper motor is drill-tapped, and the extension is attached to this face to elongate the length of the shaft. Locite threadlocker 242 solution is used to temporarily secure the extension to avoid any relative motion between the rotating components. Additionally, the sampler is rotated in clockwise direction to avoid any changes of slip between the threads.

The compact miter gearbox, with motor-shaft extension on the input shaft, is bolted down onto the (tack-welded) gearbox anchor. The stepper motor is then installed to the gearbox anchor-drive train assembly, upon coating the other end of the motor extension shaft with the thread-locker solution. Finally, the shaft extension is threaded onto the motor exit shaft such that the shoulder of the shaft extension is flushed with the cross-sectional plane of the stepper motor shaft.

Upon mounting all these components, the stepper motor is grounded to the body of the extension chamber, A grafoil seal is custom cut to the cross-section of the extension chamber and installed in between the two halves of the chamber extension. After this, the control and communication wires of stepper motor are passed through the split gland conax fittings (on the rear half of the extension chamber). At last, the two halves of the extension chamber are secured in position using a 3.75 inch long 1/4-20 brass bolts.

APPENDIX B

ENGINEERING DRAWINGS

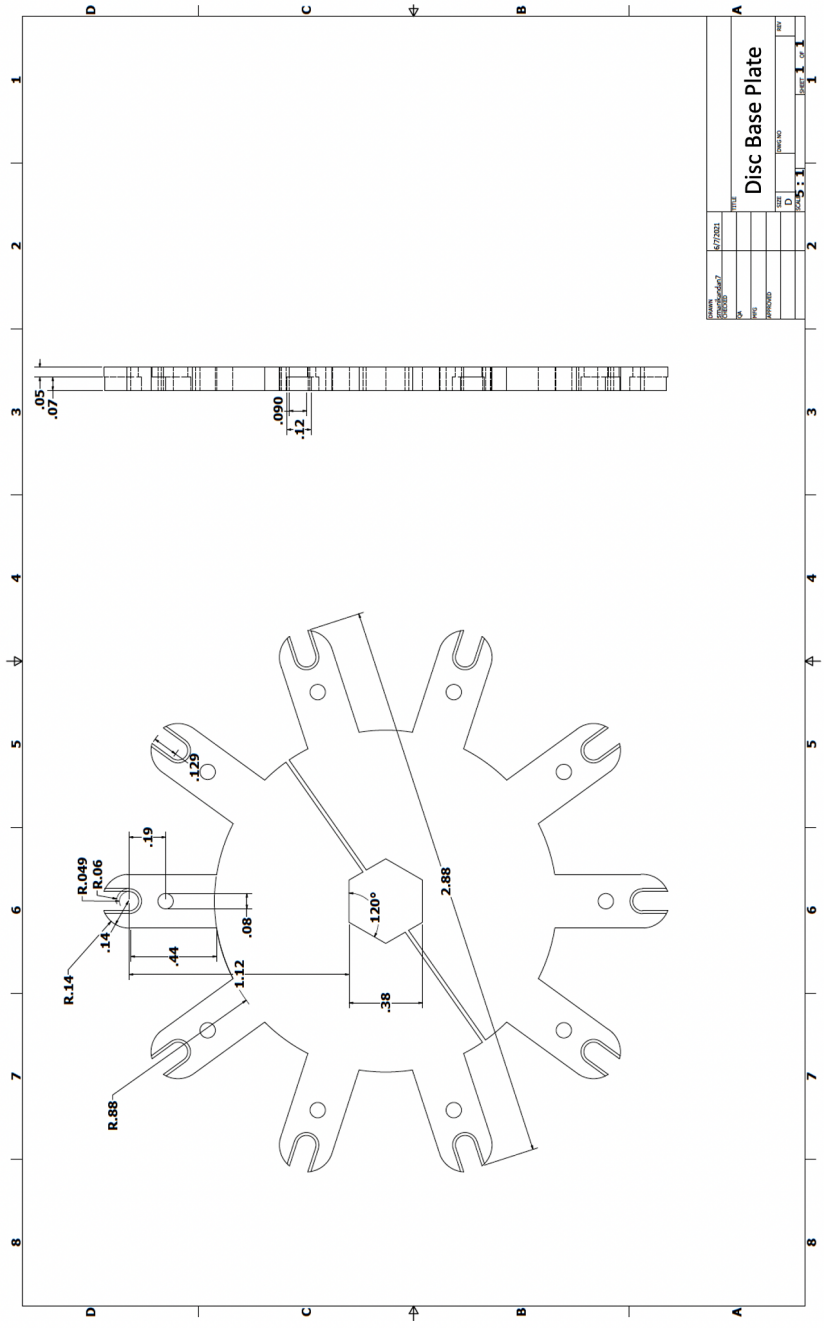

Figure B.1: Drawing of the sampling disc base plate.

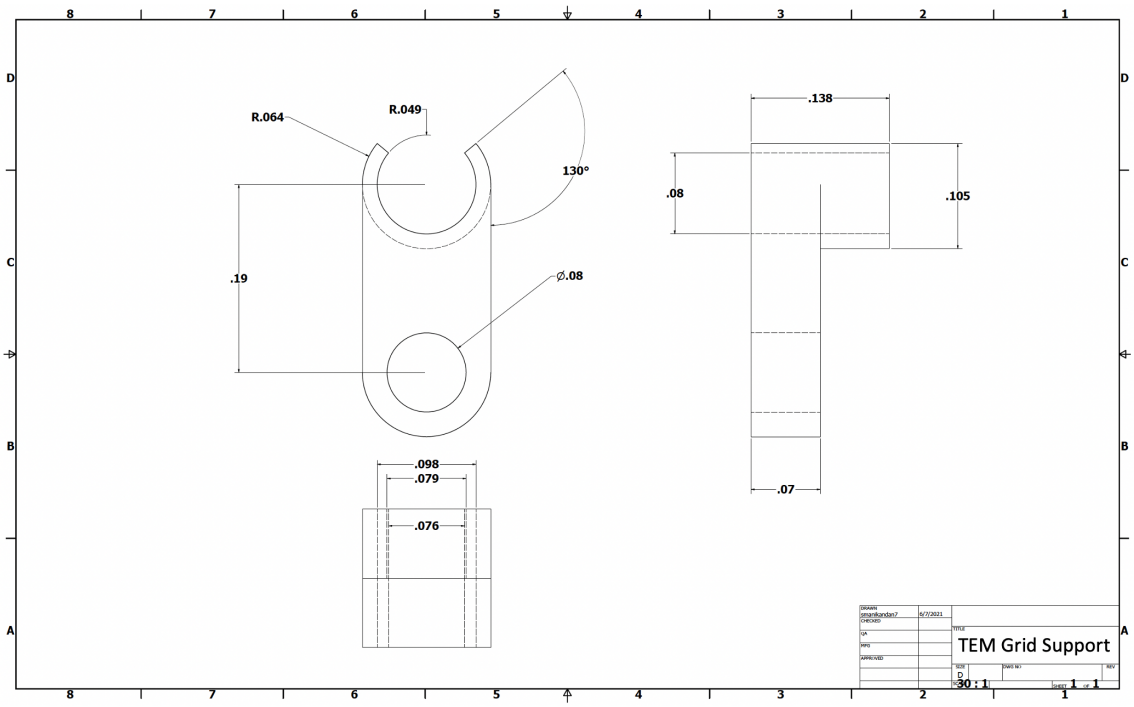

Figure B.2: Drawing of the TEM grid support.

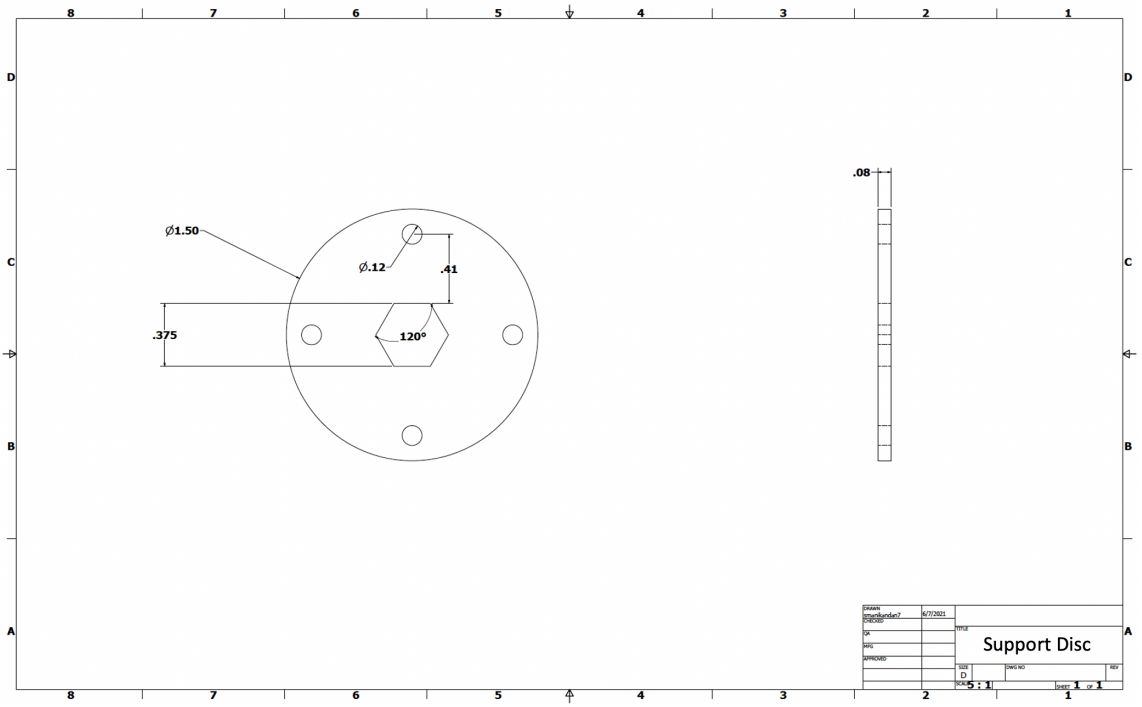

Figure B.3: Drawing of the base plate support disc.

REFERENCES

[1] M. Stettler, S. Eastham, and S. Barrett, "Air quality and public health impacts of uk airports. part i: Emissions," *Atmospheric Environment*, vol. 45, pp. 5415–5424, 31 Oct. 2011.

[2] J. Quaas, "The soot factor," *Nature*, vol. 471, pp. 456–457, 7339 Mar. 2011.

[3] J. Hansen and L. Nazarenko, "Soot climate forcing via snow and ice albedos," *Proceedings of the National Academy of Sciences*, vol. 101, pp. 423–428, 2 Jan. 2004.

[4] K. M. Bendtsen, E. Bengtsen, A. T. Saber, and U. Vogel, "A review of health effects associated with exposure to jet engine emissions in and around airports," *Environmental Health*, vol. 20, p. 10, 1 Dec. 2021.

[5] T. H. Painter, M. G. Flanner, G. Kaser, B. Marzeion, R. A. VanCuren, and W. Abdalati, "End of the little ice age in the alps forced by industrial black carbon," *Proceedings of the National Academy of Sciences*, vol. 110, pp. 15 216–15 221, 38 Sep. 2013.

[6] S. R. Turns, *An Introduction to Combustion: Concepts and Applications*, 3rd ed. McGraw-Hill, Jan. 2011.

[7] R. A. Dobbins and C. M. Megaridis, "Morphology of flame-generated soot as determined by thermophoretic sampling," *Langmuir*, vol. 3, pp. 254–259, 2 Mar. 1987.

[8] M. L. Botero, J. Akroyd, D. Chen, M. Kraft, and J. R. Agudelo, "On the thermophoretic sampling and tem-based characterisation of soot particles in flames," *Carbon*, vol. 171, pp. 711–722, Jan. 2021.

[9] T. K. A., "Soot formation in annular non-premixed laminar fames of methane- air at pressures of 0.1 to 4.0 mpa," University of Waterloo, 2004.

[10] R. Puri, R. J. Santoro, and K. C. Smyth, "The oxidation of soot and carbon monoxide in hydrocarbon diffusion flames," *Combustion and Flame*, vol. 97, pp. 125–144, 2 May 1994.

[11] R. Santoro, H. Semerjian, and R. Dobbins, "Soot particle measurements in diffusion flames," *Combustion and Flame*, vol. 51, pp. 203–218, Jan. 1983.

[12] V. A.M., "Design and development of a thermophoretic soot sampling system for high pressure laminar diffusion flames," University of Toronto, 2016.

[13] E. F. Durand, A. P. Crayford, and M. Johnson, "Experimental validation of thermophoretic and bend nanoparticle loss for a regulatory prescribed aircraft nvpm sampling system," *Aerosol Science and Technology*, vol. 54, pp. 1019–1033, 9 Sep. 2020.

[14] Köylü and G. M. Faeth, "Optical properties of soot in buoyant laminar diffusion flames," *Journal of Heat Transfer*, vol. 116, pp. 971–979, 4 Nov. 1994.

[15] M. Gu, F. Liu, J.-L. Consalvi, and O. L. Gülder, "Effects of pressure on soot formation in laminar coflow methane/air diffusion flames doped with n-heptane and toluene between 2 and 8 atm," *Proceedings of the Combustion Institute*, vol. 38, pp. 1403–1412, 1 2021.

[16] F. A. Smith and S. F. Pickering, "Bunsen flames of unusual structure," *Bureau of Standards Journal of Research*, vol. 3, pp. 65–80, 1 Jul. 1929.

[17] S. Sohrab and C. Law, "Influence of burner rim aerodynamics on polyhedral flames and flame stabilization," *Combustion and Flame*, vol. 62, no. 3, pp. 243–254, 1985.

[18] Y. Li, Y. Jiang, W. Xu, and K. Liew, "Laminar burning velocity and cellular instability of 2-butanone-air flames at elevated pressures," *Fuel*, vol. 316, p. 123 390, 2022.

[19] G. I. Sivashinsky, "On the intrinsic dynamics of premixed flames," *Philosophical Transactions: Physical Sciences and Engineering*, vol. 332, pp. 135–148, 1624 1990.

[20] S. Ishizuka and C. K. Law, "An experimental study on extinction and stability of stretched premixed flames," *Symposium (International) on Combustion*, vol. 19, pp. 327–335, 1 Jan. 1982.

[21] G. Joulin, "Flame oscillations induced by conductive losses to a flat burner," *Combustion and Flame*, vol. 46, pp. 271–281, Jan. 1982.

[22] S. B. Margolis, "Effects of selective diffusion on the stability of burner-stabilized premixed flames," *Symposium (International) on Combustion*, vol. 18, pp. 679–693, 1 1981.

[23] Z. A. Mansurov, "Soot formation in combustion processes (review)," *Combustion, Explosion, and Shock Waves*, vol. 41, pp. 727–744, 6 Nov. 2005.

[24] H. Wang, "Formation of nascent soot and other condensed-phase materials in flames," *Proceedings of the Combustion Institute*, vol. 33, pp. 41–67, 1 2011.

[25] M. Bouvier, G. Cabot, J. Yon, and F. Grisch, "On the use of piv, lii, pah-plif and oh-plif for the study of soot formation and flame structure in a swirl stratified premixed

ethylene/air flame," *Proceedings of the Combustion Institute*, vol. 38, pp. 1851–1858, 1 2021.

[26] M. Frenklach, "Reaction mechanism of soot formation in flames," *Physical Chemistry Chemical Physics*, vol. 4, pp. 2028–2037, 11 May 2002.

[27] M. Frenklach and H. Wang, "Detailed modeling of soot particle nucleation and growth," *Symposium (International) on Combustion*, vol. 23, pp. 1559–1566, 1 Jan. 1991.

[28] R. P. Bambha and H. A. Michelsen, "Effects of aggregate morphology and size on laser-induced incandescence and scattering from black carbon (mature soot)," *Journal of Aerosol Science*, vol. 88, pp. 159–181, Oct. 2015.

[29] E. Weingartner, H. Burtscher, and U. Baltensperger, "Hygroscopic properties of carbon and diesel soot particles," *Atmospheric Environment*, vol. 31, pp. 2311–2327, 15 Aug. 1997.

[30] X. Ma, C. D. Zangmeister, J. Gigault, G. W. Mulholland, and M. R. Zachariah, "Soot aggregate restructuring during water processing," *Journal of Aerosol Science*, vol. 66, pp. 209–219, Dec. 2013.

[31] O. Y. Enekwizu, A. Hasani, and A. F. Khalizov, "Vapor condensation and coating evaporation are both responsible for soot aggregate restructuring," *Environmental Science & Technology*, vol. 55, pp. 8622–8630, 13 Jul. 2021.

[32] E. G. Schnitzler, A. Dutt, A. M. Charbonneau, J. S. Olfert, and W. J§ger, "Soot aggregate restructuring due to coatings of secondary organic aerosol derived from aromatic precursors," *Environmental Science & Technology*, vol. 48, pp. 14 309–14 316, 24 Dec. 2014.

[33] K. K. Leung, E. G. Schnitzler, R. Dastanpour, S. N. Rogak, W. J§ger, and J. S. Olfert, "Relationship between coating-induced soot aggregate restructuring and primary particle number," *Environmental Science & Technology*, vol. 51, pp. 8376–8383, 15 Aug. 2017.

[34] C. Chen *et al.*, "An unexpected restructuring of combustion soot aggregates by subnanometer coatings of polycyclic aromatic hydrocarbons," *Geophysical Research Letters*, vol. 43, 20 Oct. 2016.

[35] J. Pagels, A. F. Khalizov, P. H. McMurry, and R. Y. Zhang, "Processing of soot by controlled sulphuric acid and water condensationäîmass and mobility relationship," *Aerosol Science and Technology*, vol. 43, pp. 629–640, 7 Jun. 2009.

[36] C. Qiu, A. F. Khalizov, and R. Zhang, "Soot aging from oh-initiated oxidation of toluene," *Environmental Science & Technology*, vol. 46, pp. 9464–9472, 17 Sep. 2012.

[37] H. Xue, A. F. Khalizov, L. Wang, J. Zheng, and R. Zhang, "Effects of coating of dicarboxylic acids on the massàímobility relationship of soot particles," *Environmental Science & Technology*, vol. 43, pp. 2787–2792, 8 Apr. 2009.

[38] A. Baldelli *et al.*, "Typical and atypical morphology of non-volatile particles from a diesel and natural gas marine engine," *Aerosol and Air Quality Research*, vol. 20, pp. 730–740, 4 2020.

[39] S. Bernard *et al.*, *Fib-sem and tem investigations of an organic-rich shale maturation series from the lower toarcian posidonia shale, germany <subtitle >nanoscale pore system and fluid-rock interactions</subtitle>* 2013.

[40] W. Kim, C. M. Sorensen, D. Fry, and A. Chakrabarti, "Soot aggregates, superaggregates and gel-like networks in laminar diffusion flames," *Journal of Aerosol Science*, vol. 37, pp. 386–401, 3 Mar. 2006.

[41] R. K. Chakrabarty, H. Moosmºller, M. A. Garro, and C. B. Stipe, "Observation of superaggregates from a reversed gravity low-sooting flame," *Aerosol Science and Technology*, vol. 46, pp. i–iii, 1 Jan. 2012.

[42] J. Xing *et al.*, "Morphology and composition of particles emitted from a port fuel injection gasoline vehicle under real-world driving test cycles," *Journal of Environmental Sciences*, vol. 76, pp. 339–348, Feb. 2019.

[43] A. L. Rocca, G. D. Liberto, P. Shayler, and M. Fay, "The nanostructure of soot-in-oil particles and agglomerates from an automotive diesel engine," *Tribology International*, vol. 61, pp. 80–87, May 2013.

[44] A. M. Steinberg, *Laser induced incandescence and other particle diagnostics*, 2021*.

[45] F. Liu, G. J. Smallwood, and D. R. Snelling, "Effects of primary particle diameter and aggregate size distribution on the temperature of soot particles heated by pulsed lasers," *Journal of Quantitative Spectroscopy and Radiative Transfer*, vol. 93, no. 1-3 SPEC. ISS. 2005.

[46] F. Liu, K. J. Daun, D. R. Snelling, and G. J. Smallwood, "Heat conduction from a spherical nano-particle: Status of modeling heat conduction in laser-induced incandescence," *Applied Physics B: Lasers and Optics*, vol. 83, no. 3, pp. 355–382, 2006.

[47] A. V. Filippov and D. E. Rosner, "Energy transfer between an aerosol particle and gas at high temperature ratios in the Knudsen transition regime," *International Journal of Heat and Mass Transfer*, vol. 43, no. 1, 2000.

[48] D. R. Snelling, F. Liu, G. J. Smallwood, and Ö. L. Gülder, "Determination of the soot absorption function and thermal accommodation coefficient using low-fluence LII in a laminar coflow ethylene diffusion flame," *Combustion and Flame*, vol. 136, no. 1-2, 2004.

[49] A. M. Brasil, T. L. Farias, and M. G. Carvalho, "A recipe for image characterization of fractal-like aggregates," *Journal of Aerosol Science*, vol. 30, no. 10, 1999.

[50] E. E. Michaelides, "Brownian movement and thermophoresis of nanoparticles in liquids," *International Journal of Heat and Mass Transfer*, vol. 81, pp. 179–187, 2015.

[51] A. D. Eisner and D. E. Rosner, "Experimental studies of soot particle thermophoresis in nonisothermal combustion gases using thermocouple response techniques," *Combustion and Flame*, vol. 61, no. 2, pp. 153–166, 1985.

[52] Ü. Ö. Köylü, C. S. McEnally, D. E. Rosner, and L. D. Pfefferle, "Simultaneous measurements of soot volume fraction and particle size/microstructure in flames using a thermophoretic sampling technique," *Combustion and Flame*, vol. 110, no. 4, pp. 494–507, 1997.

[53] A. Messerer, R. Niessner, and U. Pöschl, "Thermophoretic deposition of soot aerosol particles under experimental conditions relevant for modern diesel engine exhaust gas systems," *Journal of Aerosol Science*, vol. 34, no. 8, pp. 1009–1021, 2003.

[54] D. E. Rosner and Y. F. Khalil, "Particle morphology-and knudsen transition-effects on thermophoretically dominated total mass deposition rates from "coagulation-aged" aerosol population," *Journal of aerosol science*, vol. 31, no. 3, pp. 273–292, 2000.

[55] D. Rosner, D. Mackowski, and P. Garcia-Ybarra, "Size-and structure-lnsensitivity of the thermophoretic transport of aggregated "soot" particles in gases," *Combustion Science and technology*, vol. 80, no. 1-3, pp. 87–101, 1991.

[56] A. M. Vargas and Ö. L. Gülder, "A multi-probe thermophoretic soot sampling system for high-pressure diffusion flames," *Review of Scientific Instruments*, vol. 87, no. 5, p. 055 101, 2016.

[57] M. Leschowski, T. Dreier, and C. Schulz, "An automated thermophoretic soot sampling device for laboratory-scale high-pressure flames," *Review of Scientific Instruments*, vol. 85, no. 4, p. 045 103, 2014.

[58] J. Cai, N. Lu, and C. Sorensen, "Comparison of size and morphology of soot aggregates as determined by light scattering and electron microscope analysis," *Langmuir*, vol. 9, no. 11, pp. 2861–2867, 1993.

[59] C. Fuller *et al.*, "Effects of vitiation and pressure on laminar flame speeds of n-decane," American Institute of Aeronautics and Astronautics, Jan. 2012, ISBN: 978-1-60086-936-5.

[60] X. Gao *et al.*, "The effect of ozone addition on flame propagation," American Institute of Aeronautics and Astronautics, Jan. 2015, ISBN: 978-1-62410-343-8.

[61] X. Gao *et al.*, "The effect of ozone addition on laminar flame speed," *Combustion and Flame*, vol. 162, pp. 3914–3924, 10 Oct. 2015.

[62] S. Adusumilli and J. Seitzman, "Laminar flame speed measurements of ethylene at high preheat temperatures and for diluted oxidizers," *Combustion and Flame*, vol. 233, p. 111 564, Nov. 2021.

[63] S. Adusumilli, "Effects of preheat temperature and vitiation on reaction kinetics of higher hydrocarbon fuels," Georgia Institute of Technology, 2019.

[64] Y. Chen *et al.*, "Single-camera, single-shot, time-resolved laser-induced incandescence decay imaging," *Optics Letters*, vol. 43, p. 5363, 21 Nov. 2018.

[65] S. Kook *et al.*, "Automated detection of primary particles from transmission electron microscope (tem) images of soot aggregates in diesel engine environments," *SAE International Journal of Engines*, vol. 9, pp. 2015-01–1991, 1 Sep. 2015.

[66] H. Wiinikka, F. S. Hage, Q. M. Ramasse, and P. Toth, "Spatial distribution of metallic heteroatoms in soot nanostructure mapped by aberration-corrected stem-eels," *Carbon*, vol. 173, pp. 953–967, Mar. 2021.

[67] T. Aizawa *et al.*, "Transmission electron microscopy of soot particles directly sampled in diesel spray flame - a comparison between us#2 and biodiesel soot," *SAE International Journal of Fuels and Lubricants*, vol. 5, pp. 2012-01–0695, 2 Apr. 2012.

[68] Y. Liao, "Practical electron microscopy and database," *An Online Book*, 2006.

[69] S. Ishizuka, K. Miyasaka, and C. Law, "Effects of heat loss, preferential diffusion, and flame stretch on flame-front instability and extinction of propane/air mixtures," *Combustion and Flame*, vol. 45, pp. 293–308, 1982.

[70] X. Hu *et al.*, "Morphological and nanostructure characteristics of soot particles emitted from a jet-stirred reactor burning aviation fuel," *Combustion and Flame*, vol. 236, p. 111 760, 2022.

[71] W. Wang *et al.*, "Characteristics of individual particles emitted from an experimental burning chamber with coal from the lung cancer area of xuanwei, china," *Aerosol and Air Quality Research*, vol. 19, no. 2, pp. 355–363, 2019.

[72] A. Clague, J. Donnet, T. Wang, and J. Peng, "A comparison of diesel engine soot with carbon black," *Carbon*, vol. 37, no. 10, pp. 1553–1565, 1999.

[73] T. Gonet and B. A. Maher, "Airborne, vehicle-derived fe-bearing nanoparticles in the urban environment: A review," *Environmental Science & Technology*, vol. 53, no. 17, pp. 9970–9991, 2019.

[74] Y. Zhang *et al.*, "Direct observations of fine primary particles from residential coal burning: Insights into their morphology, composition, and hygroscopicity," *Journal of Geophysical Research: Atmospheres*, vol. 123, no. 22, pp. 12–964, 2018.

[75] H. S. Jung, A. Miller, K. Park, and D. B. Kittelson, "Carbon nanotubes among diesel exhaust particles: Real samples or contaminants?" *Journal of the Air & Waste Management Association*, vol. 63, pp. 1199–1204, 10 Oct. 2013.

[76] J. J. Swanson, R. Febo, A. M. Boies, and D. B. Kittelson, "Fuel sulfur and iron additives contribute to the formation of carbon nanotube-like structures in an internal combustion engine," *Environmental Science & Technology Letters*, vol. 3, pp. 364–368, 10 Oct. 2016.

[77] A. Dahl *et al.*, "Traffic-generated emissions of ultrafine particles from pavement–tire interface," *Atmospheric Environment*, vol. 40, no. 7, pp. 1314–1323, 2006.

[78] W. Li *et al.*, "A review of single aerosol particle studies in the atmosphere of east asia: Morphology, mixing state, source, and heterogeneous reactions," *Journal of Cleaner Production*, vol. 112, pp. 1330–1349, 2016.

[79] Y. Zhang *et al.*, "The soot particle formation process inside the piston bowl of a small-bore diesel engine," *Combustion and Flame*, vol. 185, pp. 278–291, Nov. 2017.

[80] X. Wang, Y. Wang, Y. Bai, P. Wang, D. Wang, and F. Guo, "Effects of 2, 5-dimethylfuran addition on morphology, nanostructure and oxidation reactivity of diesel exhaust particles," *Fuel*, vol. 253, pp. 731–740, 2019.

[81] J. Wei *et al.*, "Morphology analysis of soot particles from a modern diesel engine fueled with different types of oxygenated fuels," *Fuel*, vol. 267, p. 117 248, 2020.

[82] X. Man, C. S. Cheung, and Z. Ning, "Effect of diesel engine operating conditions on the particulate size, nanostructure and oxidation properties when using wasting cooking oil biodiesel," *Energy Procedia*, vol. 66, pp. 37–40, 2015.

[83] Q. Zhou, Y. Wang, X. Wang, and Y. Bai, "Experimental investigation into the oxidation reactivity, morphology and graphitization of soot particles from diesel/n-octanol mixtures," *Journal of Environmental Sciences*, vol. 112, pp. 218–230, 2022.

[84] C. D. Zangmeister *et al.*, "Packing density of rigid aggregates is independent of scale," *Proceedings of the National Academy of Sciences*, vol. 111, no. 25, pp. 9037–9041, 2014. eprint: https://www.pnas.org/doi/pdf/10.1073/pnas.1403768111.

[85] B. Miljevic, N. C. Surawski, T. Bostrom, and Z. D. Ristovski, "Restructuring of carbonaceous particles upon exposure to organic and water vapours," *Journal of Aerosol Science*, vol. 47, pp. 48–57, 2012.

[86] X. Pei *et al.*, "Morphological transformation of soot: Investigation of microphysical processes during the condensation of sulfuric acid and limonene ozonolysis product vapors," *Atmospheric Chemistry and Physics*, vol. 18, no. 13, pp. 9845–9860, 2018.